Schilder, F., Vogt, W., Schreiber, S., & Osinga, H. M. (2005). Fourier methods for quasi-periodic oscillations.

Early version, also known as pre-print

University of Bristol - Explore Bristol Research
General rights

Fourier methods for quasi-periodic oscillations

Frank Schilder*   Werner Vogt   Stephan Schreiber
Hinke M. Osinga

11th January 2005

Abstract

Quasi-periodic oscillations and invariant tori play an important role in the study of forced or coupled oscillators. This paper presents two new numerical methods for the investigation of quasi-periodic oscillations. Both algorithms can be regarded as generalisations of the averaging and the harmonic (spectral) balance methods. The algorithms are easy to implement and require only minimal a-priory knowledge of the system. In particular, the methods do not depend on an a-priory coordinate transformation. The methods are applied to a number of illustrative examples from nonlinear electrical engineering and the results show that the methods are efficient and reliable. In addition, these examples show that the presented algorithms can also continue through regions of sub-harmonic (phase-locked) resonance even though they are designed only for the quasi-periodic case.

Key words. quasi-periodic oscillation, averaging method, Fourier method, invariant torus, Van der Pol oscillator

Copyright

Contents

---

1   Introduction

The existence of steady (that is, non-transient) responses that are non-periodic
has long been established in many diverse engineering systems. In particular,
quasi-periodic responses are the simples form of output in quasi-periodically
forced systems with forcing terms that contain different, incommensurate fre-
quencies; see, for example, [1, 2, 3]. A quasi-periodic solution of a nonlinear
system is a motion that, in the simplest case, takes place on a two-dimensional
torus (in phase space) that is associated with two incommensurate internal fre-
quencies. To understand the response output of such systems in the presence of
nonlinearity, it is necessary to have a robust method for the computation and
parameter-continuation of such tori.

 We consider the computation and continuation of quasi-periodic solutions
of model systems comprising periodically forced ordinary differential equations
(ODEs) of the form

$$\dot{x} = f(x, t, \lambda), \qquad x \in \mathbb{R}^n, \ t, \lambda \in \mathbb{R}, \ n \geq 2, \qquad (1)$$

where $f : \mathbb{R}^n \times \mathbb{R} \times \mathbb{R} \to \mathbb{R}^n$ is sufficiently smooth and periodic in t. The
parameter λ plays the role of a free parameter and we assume that (1) has
invariant tori for an interval of λ-values. Our goal is to follow the invariant tori

of (1) as a function of λ, that is, we want to numerically approximate a branch of invariant tori in combined phase and parameter space, until the torus breaks down and no longer exists as a smooth invariant object; we refer to [4, 5, 6, 7] for examples of how invariant tori can cease to exist.

In general, a quasi-periodic oscillation that is associated with p different internal frequencies takes place on a p-dimensional invariant torus. In fact, the quasi-periodic oscillation densely covers the invariant torus so that it can be observed in an experiment. We call such a torus a *quasi-periodic invariant torus*. Suppose that System (1) has a locally unique quasi-periodic solution and, thus, a quasi-periodic invariant torus for some parameter value $\lambda = \lambda_0$. If we perturb the parameter λ slightly, then the torus will typically persist as an invariant torus, but the solution curves on the torus may not be quasi-periodic but *phase-locked*, that is, in sub-harmonic resonance. More precisely, if we vary the parameter λ in some interval $\lambda \in [a, b]$, we typically find quasi-periodic oscillations only for parameter values in a Cantor set of positive measure and for all other parameter values the solutions are phase-locked [6, 8, 7]. Thus, quasi-periodic oscillations are a rather delicate object to study and one usually tries to analyse the underlying (more robust) invariant torus instead. We follow this line throughout this paper and use the terms quasi-periodic oscillation and quasi-periodic invariant torus as well as phase-locked oscillation and phase-locked invariant torus interchangeably.

In the next section we give a brief summary of important properties of quasi-periodic solutions and invariant tori; see also [9].

1.1 Quasi-Periodic Oscillations and Invariant Tori

Any quasi-periodic solution $x(t)$ can be expressed as a function $x(t) = u(\omega t)$, where $u(\theta)$ is a *torus function*, that is, the function u is defined on the p-dimensional square $\mathbb{T}^p := [0, 2\pi]^p$ and is 2π-periodic in each of the variables θ_i, $i = 1, \ldots, p$. We say that a torus function u is r times continuously differentiable if the partial derivatives $\prod_{i=1}^{p}(\partial/\partial\theta_i)^{\alpha_i} u$ are continuous torus functions for all integers $\alpha_i \geq 0$ with $\sum_{i=1}^{p} \alpha_i \leq r$. The real numbers ω_i, $i = 1, \ldots, p$, are called the *basic frequencies* of the quasi-periodic function $x(t)$ and the tuple $\omega = (\omega_1, \ldots, \omega_p)$ is called the *frequency base*. Since the function x is quasi-periodic, the basic frequencies ω_i must be *incommensurate* (*rationally independent*), that is, for integers k_i the equation $\langle k, \omega \rangle := \sum_{i=1}^{p} k_i \omega_i = 0$ holds if and only if all $k_i = 0$ for $i = 1, \ldots, p$. For $p = 2$ this means that the ratio ω_1/ω_2 is irrational. Without loss of generality we may set $\omega_1 = 1$ because Equation (1) can always be transformed such that the forcing period $T_1 := 2\pi/\omega_1$ becomes $T_1 = 2\pi$. Unless otherwise stated we use the term quasi-periodic function for a quasi-periodic function with a two-dimensional frequency base.

A quasi-periodic function with p-dimensional frequency base ω can uniformly be approximated by quasi-trigonometric polynomials:

$$x(t) = \sum_{k \in \mathbb{Z}^p} c_k e^{j\langle k, \omega \rangle t}, \qquad c_k := \lim_{a \to \infty} \frac{1}{2a} \int_{-a}^{a} x(t) e^{-j\langle k, \omega \rangle t}\, dt, \qquad (2)$$

where $j = \sqrt{-1}$ denotes the imaginary unit. The associated torus function u, $x(t) = u(\omega t)$, can uniformly be approximated by trigonometric polynomials in

the p angular variables θ_i, $i = 1, \ldots, p$:

$$u(\theta) = \sum_{k \in \mathbb{Z}^p} c_k e^{j\langle k, \theta \rangle}, \qquad c_k := \frac{1}{(2\pi)^p} \int_{\mathbb{T}^p} u(\theta) e^{-j\langle k, \theta \rangle} \, d\theta. \tag{3}$$

Note that, for incommensurate ω, the Mean Value Theorem [9] guarantees that the Fourier coefficients c_k are the same for a quasi-periodic function x and its associated torus function u. However, even though these Fourier coefficients are identical, there is an important difference for practical computations. Namely, the computation of the Fourier coefficients in (2) involves a limit process and an integration over an infinite domain, which is hard to handle numerically, while the integration in (3) is performed over a finite domain and can be done using standard algorithms.

The requirement that ω be incommensurate cannot be omitted. To see this, consider the case $p = 2$ and let us assume that $\varrho = \omega_1/\omega_2 = p/q$ is a rational number, where p and q are relatively prime integers. Then, there exist integers k and l such that $k\omega_1 + l\omega_2 = 0$ holds, for example, for $k = q$ and $l = -p$. This implies that with $k = \kappa + mq$ and $l = \lambda - mp$ we have $\exp((\kappa+mq)\omega_1+(\lambda-mp)\omega_2) = \exp(\kappa\omega_1+\lambda\omega_2+m(q\omega_1-p\omega_2)) = \exp(\kappa\omega_1+\lambda\omega_2)$, where κ, λ and m are arbitrary integers. In other words, the Fourier coefficients $c_{\kappa+mq, \lambda-mp}$ are all the same for fixed κ and λ, and arbitrary m. Since κ and λ can be chosen freely, it follows, that *each value $c_{kl} \exp(k\omega_1 + l\omega_2)$ occurs infinitely many times in the Fourier series (2)*. Thus, the series (2) does not, in general, converge for rational $\varrho = \omega_1/\omega_2 = p/q$.

If $x(t)$ is a quasi-periodic solution with p-dimensional frequency base ω of the autonomous system $\dot{x} = f(x)$, $x \in \mathbb{R}^n$, its associated torus function $u(\theta)$ is a solution of the so-called invariance condition

$$\sum_{i=1}^{p} \omega_i \frac{\partial u}{\partial \theta_i} = f(u), \tag{4}$$

as was earlier shown in [10]. This partial differential equation (PDE) states that $f(u(\theta))$ must be tangent to $u(\theta)$. The invariance condition (4) does not define a unique solution. This is due to the fact that for any solution $u(\theta)$ of (4) also $v(\theta) := u(\theta + \beta)$ satisfies the invariance condition for arbitrary but fixed phase shifts $\beta \in \mathbb{R}^p$, the solution u has p free phases. One way to obtain a unique solution is to fix the free phases by supplementing the invariance condition (4) by the p so-called *phase conditions*

$$\left\langle \frac{\partial \tilde{u}}{\partial \theta_i} \, , \, u \right\rangle_{\mathcal{L}_2^n} = 0, \qquad i = 1, \ldots, p, \tag{5}$$

where $\tilde{u}$ is an a-priori known approximation from, for example, a simulation, an initial guess or a continuation process. Here,

$$\langle u \, , \, v \rangle_{\mathcal{L}_2^n} := \frac{1}{(2\pi)^p} \int_{\mathbb{T}^p} \langle u(\theta) \, , \, v(\theta) \rangle_{\mathbb{C}^n} \, d\theta, \qquad \langle x \, , \, y \rangle_{\mathbb{C}^n} := \sum_{i=1}^{n} x_i \overline{y}_i,$$

denotes the inner product in $\mathcal{L}_2^n$. In particular, in the case of periodic solutions of autonomous ODEs, Equation (5) becomes the well-known integral phase condition used, for example, in MATCONT [11] and AUTO [12].
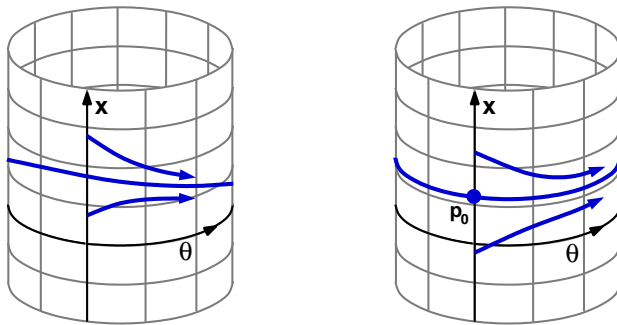
Figure 1: Interpretation of a periodically forced system in the cylindrical phase space $\mathbb{R}^n \times S^1$. A periodic response forms a closed curve (left). The variables x and θ can be decoupled by averaging. In the averaged system the periodic response becomes the circle $p_0 \times S^1$ (right).

1.2   Outline

This paper is organised as follows. In the next section, we review the well-known averaging method that is used to investigate periodic or quasi-periodic solutions of periodically forced ODEs. The averaging method uses an approximation of the system that is simpler to analyse and often leads to good predictions of the behaviour of the original system. We introduce the technique of averaging in a such a way that it is immediately clear how the methods proposed in this paper relate to this well-known technique. There are two different algorithms that we discuss in this paper. The semi-discretisation method presented in Section 3 is a direct generalisation of solving periodic orbits using the invariance equation and appropriate phase conditions (4)-(5). In Section 4 this method is tested with two examples, namely, a parametrically forced network and an electrical circuit with saturable inductors. Section 5 describes the full-discretisation method, which uses the approach of solving the under-determined equation (4) using a pseudo inverse operator. This method is tested on the same examples as the semi-discretisation method, and also on an example of two coupled Van der Pol oscillators, for which the semi-discretisation method cannot be used; see Section 6. The main conclusions can be found in Section 7.

2   The Averaging Method

Since our approach for finding quasi-periodic solutions can be interpreted as a generalisation of the averaging method, we briefly discuss the averaging method here. A general introduction can be found, for example, in [13, 14, 15, 16]. We specifically focus on the averaging method in the context of the numerical approximation of periodic and quasi-periodic solutions of periodically forced ODEs, which clearly emphasises the underlying ideas for the semi-discretisation method described in Section 3.

Consider the ODE

$$\dot{x} = \varepsilon f(x, t), \qquad x \in \mathbb{R}^n, \ t \in \mathbb{R}, \ n \geq 2, \tag{6}$$

where ε is a real parameter. As in (1), we assume that time is rescaled such that f is 2π-periodic in t and twice continuously differentiable. Such an ODE is said to be in *periodic standard form* [16]. It is common practice to make Equation (6) autonomous by extending the ODE with a 2π-periodic angular variable $\theta \in S^1$:

$$\begin{aligned} \dot{x} &= \varepsilon f(x, \theta)\,, \\ \dot{\theta} &= 1\,. \end{aligned} \tag{7}$$

The phase space of (7) is the cylinder $\mathbb{R}^n \times S^1$, where S^1 is the unit circle parametrised over $[0, 2\pi)$; see Fig. 1.

The basic idea of averaging is to *decouple* the equations in (7) using a θ-average $f_0(x)$ of $f(x, \theta)$ over $[0, 2\pi]$, that is, $f_0(x) := \frac{1}{2\pi} \int_0^{2\pi} f(x, \theta)\, d\theta$. The *averaged system* of (7) is then

$$\begin{aligned} \dot{x} &= \varepsilon f_0(x)\,, \\ \dot{\theta} &= 1\,. \end{aligned} \tag{8}$$

Due to the decoupling, system (8) is usually simpler to analyse. Moreover, provided that ε is small, solutions of the averaged system (8) imply the existence of similar solutions for the original system (7). In particular, the following two theorems hold:

Theorem 1 (Periodic solutions) *If p_0 is a hyperbolic equilibrium point of $\dot{x} = \varepsilon f_0(x)$ then Equation (7) possesses a periodic solution γ_ε near $p_0 \times S^1$ for small $|\varepsilon| > 0$. The periodic solution γ_ε has the same stability type as p_0.*

Theorem 2 (Invariant tori) *If γ_0 is a hyperbolic periodic solution of $\dot{x} = \varepsilon f_0(x)$ then Equation (7) possesses an invariant 2-torus T_ε near $\gamma_0 \times S^1$ for small $|\varepsilon| > 0$. The invariant torus T_ε has the same stability type as γ_0.*

Theorem 1 is a consequence of the so-called Averaging Theorem; compare Fig. 1, and see [14, 16] for the complete theorem. The stability types of the equilibrium point p_0 and the periodic solution γ_ε are the same in the sense that if λ is an eigenvalue of the Jacobian $\partial/\partial x\, f_0(p_0)$ then γ_ε has a Floquet multiplier $\mu \approx e^\lambda$. Theorem 2 is a reformulated version of Theorem 4.4.2 in [14]. Note that Theorem 2 does not say anything about the dynamics on the invariant torus T_ε. It may be quasi-periodic which means that each solution on T_ε densely covers the entire torus, but it may also be phase-locked, that is, each solution on T_ε quickly locks to a sub-harmonic solution on T_ε and one cannot observe the torus in an experiment.

For many systems in the periodic standard form (6) it is possible to compute the averaged system explicitly, while it is hard to obtain good approximations to the Poincaré or stroboscopic map. If a system is not in periodic standard form, it can sometimes be transformed into periodic standard form. An important standard example is the weakly periodically perturbed harmonic oscillator

$$\ddot{x} + x = \varepsilon f(x, \dot{x}, t)\,, \qquad x, t \in \mathbb{R} \tag{9}$$

where again ε is a real parameter and f is 2π-periodic in t. After rewriting (9) as a first-order system and applying the transformation

$$\begin{aligned} x(t) &= a(t) \sin t + b(t) \cos t\,, \\ \dot{x}(t) &= a(t) \cos t - b(t) \sin t\,, \end{aligned} \tag{10}$$

Equation (9) assumes the periodic standard form

$$
\begin{aligned}
\dot{a} &= \varepsilon g(a, b, t) \cos t\,, \\
\dot{b} &= -\varepsilon g(a, b, t) \sin t\,,
\end{aligned}
$$

where $g(a, b, t) := f(a \sin t + b \cos t\,,\ a \cos t - b \sin t\,,\ t)$.

The main advantage of averaging is that the computation of periodic orbits is reduced to the computation of an equilibrium point of an autonomous system, which is a much simpler problem. This is even more true for the approximation of invariant tori. While there are many publicly available robust algorithms for the numerical analysis of periodic solutions, algorithms for the computation of invariant tori are still under development. Furthermore, the averaged system often reflects the qualitative behaviour of a system with astonishing accuracy even when the parameter ε is rather large.

On the other hand, the averaging method requires that a system must be in periodic standard form and have a small parameter. This heavily restricts the applicability of the averaging method as a basis for a black-box method. For systems not in periodic standard form, it is not always straightforward to find a suitable transformation. This becomes even more complicated, and is often impossible, for higher-dimensional ODEs. Furthermore, the accuracy of approximations obtained by averaging is only of order ε [14, 16]. Even though it is possible to construct higher-order methods of averaging [14, 16], one still needs the system in periodic standard form.

These problems motivate the development of tools that allow the direct investigation of systems in the general form (1). We derive the semi-discretisation method in Section 3 with the aim of combining the power of averaging with general applicability. In particular, we want to overcome the restrictions that a system must be available in a specific form and must have a small parameter. Furthermore, we want our method to be able to approximate a quasi-periodic solution with prescribed accuracy.

3 The Semi-Discretisation Method

The semi-discretisation method attempts to derive an autonomous ODE similar to the ODE obtained by averaging, starting from the general form (1). The basic idea is to use the formulation $x(t) = \sum_k y_k(t)\varphi_k(t)$, with φ_k suitable 2π-periodic functions, for the solution of a periodically forced system; this is a generalisation of (10). The goal is to obtain a system related to (1) for which quasi-periodic solutions are reduced to periodic solutions. The method is constructed in three steps: First, we show that a quasi-periodic solution can be approximated by Fourier polynomials where the coefficients are 2π-periodic functions. Using this formulation, we derive an equation for the corresponding torus function in two angular coordinates. Finally, we eliminate one of these angular coordinates by applying Galerkin's method. This process is called a semi-discretisation, because we do not obtain a finite-dimensional algebraic system, but an autonomous differential equation. Since we seek periodic solutions of the latter, we are able to apply standard algorithms for the computation of periodic solutions; see [15] for an overview.

3.1   Derivation of the Spectral System

In what follows we assume that (1) has a (locally) unique quasi-periodic solution with frequency basis $(1, \omega)$ for some parameter value $\lambda = \lambda_0$. Our goal is to separate the two time-like 'variables' t and ωt and to eliminate the explicit occurrence of t. To this end, we expand the quasi-periodic solution $x(t)$ in a Fourier series and collect the terms in ωt as follows:

$$x(t) = \sum_{k,l=-\infty}^{\infty} c_{kl} e^{j(k+l\omega)t} = \sum_{k=-\infty}^{\infty} \left(\sum_{l=-\infty}^{\infty} c_{kl} e^{jl\omega t} \right) e^{jkt} = \sum_{k=-\infty}^{\infty} y_k(\omega t)\, e^{jkt},$$

that is, a quasi-periodic function can be written as a *Fourier series in trigonometric polynomials with periodic functions as coefficients*. We call such a Fourier series a *generalised Fourier series*. The idea is now to approximate $x(t)$ by a generalised Fourier polynomial with 2π-periodic functions as coefficients:

$$x_N(t) = \sum_{k=-N}^{N} y_k(\omega t)\, e^{jkt}. \tag{11}$$

Since $x(t)$ is assumed to be a solution of (1), we have

$$\dot{x}(t) = \sum_{k=-\infty}^{\infty} \omega\, y_k'(\omega t)\, e^{jkt} + jk\, y_k(\omega t)\, e^{jkt} = f\left(\sum_{k=-\infty}^{\infty} y_k(\omega t)\, e^{jkt}, t \right).$$

Here, we omitted $\lambda = \lambda_0$ in the notation of f and $'$ denotes the derivative with respect to ωt.

Now follows the *key step*, namely, the transition to the torus system. We substitute θ_1 for t and θ_2 for ωt and obtain the equation

$$\sum_{k=-\infty}^{\infty} \omega\, y_k'(\theta_2)\, e^{jk\theta_1} + jk\, y_k(\theta_2)\, e^{jk\theta_1} = f\left(\sum_{k=-\infty}^{\infty} y_k(\theta_2)\, e^{jk\theta_1}, \theta_1 \right) \tag{12}$$

in torus coordinates. Note that the separation of variables is here a natural consequence of the transition to the torus system, we did not require a splitting into 'slow' and 'fast' variables; compare with [17, 18, 16].

Equation (12) is suited for applying the Galerkin projection onto the subspace spanned by the trigonometric polynomials $e^{jk\theta_1}$, $k = -N, \dots, 0, \dots, N$, which is defined by multiplying both sides of Equation (12) by $e^{-jk\theta_1}$ and integration over $[0, 2\pi]$ with respect to θ_1. We emphasise that this procedure is meaningful in torus coordinates only, thus, the transition to the torus system is essential. The Galerkin projection yields the autonomous system

$$\omega \begin{pmatrix} y_{-N}' \\ \vdots \\ y_0' \\ \vdots \\ y_N' \end{pmatrix} = \begin{pmatrix} f_{-N}(y) - j(-N)\, y_{-N} \\ \vdots \\ f_0(y) \\ \vdots \\ f_N(y) - jN\, y_N \end{pmatrix} \tag{13}$$

where $y := (y_{-N}, \dots, y_0, \dots, y_N)^{\mathrm{T}}$ and f_k, $k = -N, \dots, 0, \dots, N$, denotes the k-th Fourier coefficient

$$f_k(y(\theta_2)) := \frac{1}{2\pi} \int_0^{2\pi} f\left(\sum_{l=-N}^{N} y_l(\theta_2)\, e^{jl\theta_1}, \theta_1 \right) e^{-jk\theta_1}\, d\theta_1. \tag{14}$$

Since one can interpret the coefficient functions y_k as time-varying amplitudes of the first $2N+1$ Fourier modes, we refer to system (13) as the *spectral system*. The unknown frequency ω can be eliminated by applying the transformation $\theta_2 \to \omega t$. In the transformed system one seeks periodic solutions of unknown period T. In either case, the unknown frequency or period can be fixed by adding a suitable phase condition; see [12, 10]. The semi-discretisation method and in particular the transition to the torus equation can strictly be justified. Starting with the invariance equation (4)-(5) for quasi-periodic invariant tori, one can derive the exact same algorithm using the Fourier polynomial $u(\theta_1, \theta_2) = \sum_{k=-N}^{N} y_k(\theta_2)\, e^{jk\theta_1}$ for approximating the torus function u. We adopted the above treatment to emphasise the relation to averaging methods.

3.2   Properties of the Spectral System

Solutions of the spectral system (13) are related to solutions of the periodically forced ODE (1) in the sense that, as $N \to \infty$, the spectral system (13) has a 2π-periodic solution (an equilibrium point) y if and only if $x(t) = \sum_{k=-\infty}^{\infty} y_k(\omega t)e^{jkt}$ is a quasi-periodic (periodic) solution of Equation (1); compare with Theorems 1 and 2 of Section 2 for systems in periodic standard form. Note that this correspondence does not guarantee convergence, an extensive convergence analysis of Fourier-Galerkin methods for torus equations can be found in [9].

The semi-discretisation method extends the averaging method in the sense that it is applicable to general systems of the form (1) and contains the averaging method as a special case. To see this, suppose we are given an ODE in periodic standard form (6). We set up a quasi-periodic solution as the zero[th]-order Fourier polynomial $x(t) = y_0(\omega t) \cdot 1$ and apply our semi-discretisation method. The result is the spectral system $\omega y_0' = \varepsilon f_0(y_0)$ or, after the transformation $\theta_2 \to \omega t$, the system $\dot{y}_0 = \varepsilon f_0(y_0)$. The Fourier coefficient f_0 is defined by $f_0(y_0(\theta_2)) := \frac{1}{2\pi} \int_0^{2\pi} f(y_0(\theta_2) \cdot 1, \theta_1)\, d\theta_1$, thus, this particular spectral system is identical to the averaged system (8).

Since (1) is an ODE in real variables, the equalities $y_k = \overline{y}_{-k}$ and $f_k = \overline{f}_{-k}$ hold and the spectral system (13) with complex y can be transformed into a system with real $\widehat{y}$:

$$
\begin{array}{rcl}
\widehat{y}_{-k} &=& \frac{1}{2j}(y_k - y_{-k}), \quad k = 1, \ldots, N\,, \\
\widehat{y}_0 &=& y_0 \\
\widehat{y}_k &=& \frac{1}{2}(y_k + y_{-k}), \quad k = 1, \ldots, N\,.
\end{array}
$$

This transformation yields the spectral system for trigonometric polynomials of the form $x(t) = \widehat{y}_0(\omega t) + \sum_{k=1}^{N}(\widehat{y}_{-k}(\omega t)\sin kt + \widehat{y}_k(\omega t)\cos kt)$ instead of (11).

If the right-hand side of (1) is a trigonometric polynomial with polynomial coefficients, that is, f has the form $f(x, t) = \sum_k p_k(x)e^{jkt}$, where the p_k are polynomials of finite order in x, one can compute the spectral system by applying the addition theorems for trigonometric functions and comparing coefficients. This procedure is known as *harmonic balancing*. Thus, the semi-discretisation presented here can be regarded as a generalisation of the harmonic balance method [13, 15] too.

Our implementation of the semi-discretisation method is based on real trigonometric polynomials and uses harmonic balancing, hence, we assume that the

right hand side of the ODE is in trigonometric polynomial form. It is realised as symbolic algorithms in Maple and MuPad. The output of these algorithms is an autonomous ODE where ω is eliminated. This ODE in symbolic form can then be translated into an input file for the continuation package AUTO [12] or into an input file for the continuation package TORCONT [19] developed by the authors. The latter was mainly used in our examples because it is not straightforward to extract the approximation error and Fourier-mode information on which our analysis relys from the output of AUTO.

The package TORCONT computes periodic solutions of ODEs using a finite-difference approximation of order 4 on a uniform mesh. The approximation error ERR is estimated as the difference of this solution with a finite-difference solution of order 2 on the same mesh and is part of the output. With TORCONT, a periodic solution can be continued in one external parameter using a pseudo arc-length continuation algorithm with Newton's method as corrector. The user prescribes the accuracy of the correction step, which is the Euclidean norm of the last Newton correction. We usually choose a value which is smaller than the approximation error so that the error introduced by Newton's method is negligible. Note, however, that one cannot gain accuracy by choosing small correction errors, since the approximation error depends on the number of mesh-points used for the finite difference method.

In the examples we show cross-sections of the tori on which the quasi-periodic oscillation takes place. These cross-sections are straightforward to compute:

$$\gamma_1(\theta_2) = \sum_{k=-N}^{N} y_k(\theta_2)\,, \qquad \gamma_2(\theta_1) = \sum_{k=-N}^{N} y_k(0)\, e^{jk\theta_1}\,,$$

and actually approximate invariant closed curves of the period-2π and the period-$2\pi/\omega$ stroboscopic maps that can be defined near a quasi-periodic solution; see also [10].

4   Examples

We demonstrate the performance of the semi-discretisation method with two examples from nonlinear electrical engineering. Both examples were also analysed in [10] with a different algorithm. The first example, investigated in Section 4.1, is a parametrically forced network due to Philippow [20]. This example is particularly useful to examine the robustness of the semi-discretisation method, because sub-harmonic responses occur for large regions in parameter space [10].

The second example, discussed in Section 4.2, is a circuit with saturable inductors introduced by Hayashi [21]. It is possible to qualitatively analyse this system with surprising accuracy using the averaging method, which was one of the reasons for our interest in the averaging method. Specifically, it raised the question whether it is possible to use algorithms for the numerical analysis of bifurcations of periodic solutions of the semi-discretised system in order to detect quasi-periodic bifurcations. Unfortunately, it turns out that there is no simple one-to-one correspondence as will be discussed in Section 4.2. Methods for the detection of bifurcations and branch-switching are currently under development.
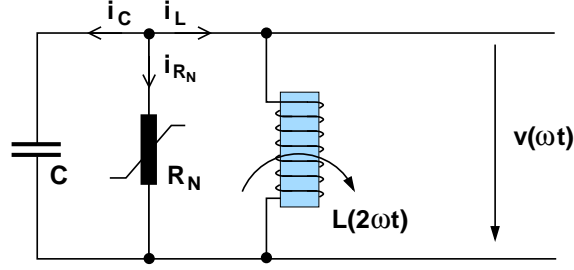
Figure 2: A parametrically forced network with a non-linear resistor and a time-dependent inductor as modelled by Equation (15). The characteristic of the resistor is approximately cubic and has regions with negative slope. The periodic forcing is due to the time-dependence of the inductance.

4.1   A Parametrically Forced Network

Our first example is the parametrically forced network depicted in Fig. 2. This circuit involves a capacitor C, a non-linear resistor R and a time-dependent inductor L and was derived by Philippow in [20] for use as a 2:1 frequency divider. A model for this circuit can be derived using the node equation

$$i_C + i_{R_N} + i_L = 0$$

where the currents i_C, i_{R_N} and i_L over each of the components are given by the expressions

$$
\begin{aligned}
i_C &= C\frac{dv}{dt}\,, \\
i_{R_N} &= b_1 v^3 - b_2 v\,, \\
i_L &= \frac{\psi}{L_0(1 + \frac{b}{2}\sin 2\omega t)} \approx \frac{\psi}{L_0}\left(1 - \frac{b}{2}\sin 2\omega t\right)\,.
\end{aligned}
$$

Here, v denotes the drop of voltage which is the same over each component. Using the relation $\frac{d\psi}{dt} = v$ for the inductance, one can derive an equation of the form

$$\ddot{x} + \alpha\dot{x}^3 - \beta\dot{x} + (1 + B\sin 2t)x = 0\,. \tag{15}$$

The value $x(t)$ is the normalised voltage and the coefficients $\alpha = \varepsilon - B$ and $\beta = \frac{\varepsilon}{2} - B$, with B and ε free real parameters, are chosen such that the system's response to the input signal $B\sin 2t$ is 2π-periodic and almost harmonic, in other words, the frequency of the input signal is halved.

4.1.1   Preliminary Analysis

For completeness, we summarise here some results of the analysis of system (15) that was carried out in [10]. To begin with, we substitute the parameter values for α and β and introduce an angular coordinate $\theta \in S^1$. Thereby, Equation (15) becomes the equivalent extended system

$$\ddot{x} + (\varepsilon - B)\dot{x}^3 - \left(\frac{\varepsilon}{2} - B\right)\dot{x} + (1 + B\sin\theta)x = 0\,, \tag{16}$$
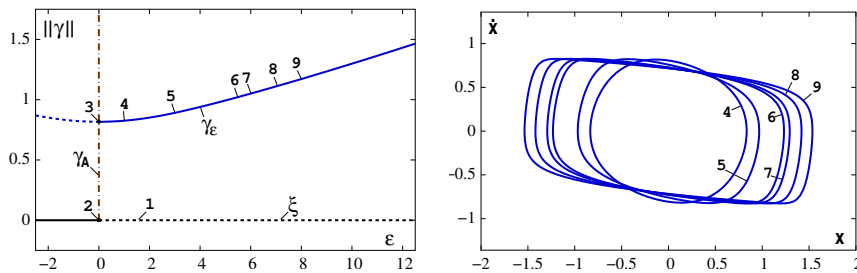
$$\dot{\theta} = 2\,, \tag{17}$$

Figure 3: The left panel shows the bifurcation diagram of (18) and the right panel displays periodic solutions of the branch γ_ε for $\varepsilon = 1.0, 3.0, 5.48, 6.0, 7.05$ and 8.0, as marked by the labels 4–9.

which allows for a straightforward geometric interpretation. Let us first consider the case $B = 0$ where no forcing is present and the variables x and θ decouple. Equation (16) then becomes the autonomous ODE

$$\ddot{x} + \varepsilon \dot{x}^3 - \frac{\varepsilon}{2}\dot{x} + x = 0\,. \tag{18}$$

The bifurcation diagram of (18) was computed with AUTO [12] and is shown in Fig. 3 (left). Equation (18) always has the equilibrium point $(x, \dot{x}) = (0, 0)$, which is attracting for $\varepsilon < 0$ and repelling for $\varepsilon > 0$. The branch ξ marked by label 1 indicates this equilibrium point and its stability type depending on ε. At $\varepsilon = 0$ (label 2), the origin loses stability in a Hopf bifurcation. Equation (18) becomes the harmonic oscillator $\ddot{x} + x = 0$, hence, a vertical branch $\gamma_A = (x, \dot{x}) = (A\cos(t - \phi_0), -A\sin(t - \phi_0))$ of neutrally stable 2π-periodic solutions with amplitude A and initial phase ϕ_0 emanates. If we continue these periodic solutions with respect to the amplitude A, then, for $A = \sqrt{2/3}$ (label 3), a branch-point is detected, where an ε-dependent branch γ_ε of periodic solutions intersects γ_A. The solutions on this branch are unstable for $\varepsilon < 0$ and attracting for $\varepsilon > 0$. Some of these solutions are shown in the right panel of Fig. 3.

Since, for $B = 0$, the Equations (16)-(17) are decoupled, the solutions of (16)-(17) are given by superposition, that is, by $(x(t), \dot{x}(t), \theta(t))$, where $(x(t), \dot{x}(t))$ denotes the solution of (16) and $\theta(t) = 2t \bmod 2\pi$ is the π-periodic solution of (17). Hence, System (16)-(17) always has the periodic solution $\gamma_0 = (x, \dot{x}, \theta) = (0, 0, 2t \bmod 2\pi)$. At $\varepsilon = 0$, a branch $T_A = (x, \dot{x}, \theta) = (A\cos(t - \phi_0), -A\sin(t - \phi_0), 2t \bmod 2\pi)$ of invariant tori emanates in a torus (Neimark-Sacker) bifurcation. These tori can be parametrised by t and ϕ_0 and, since the two basic frequencies $\omega_1 = 2$ and $\omega_2 = 1$ are in sub-harmonic resonance, all of these tori are covered by 2π-periodic solutions which wind twice around the torus. At amplitude $A = \sqrt{2/3}$, an ε-dependent branch T_ε of invariant tori emerges from T_A. This time, the second basic frequency ω_2 varies with ε. Thus, the tori are either covered by periodic or quasi-periodic solutions for rational or irrational values of ω_2/ω_1, respectively.

In our subsequent investigation, we focus on the branch T_ε and parameter values $\varepsilon > 0$, since for these values the invariant tori of T_ε are attracting and can, for comparison, be visualised by simulation. From dynamical systems theory it is known that, for small forcing amplitudes $B > 0$, the attracting invariant tori of T_ε will survive as tori [23], but the solutions on these tori are quasi-periodic
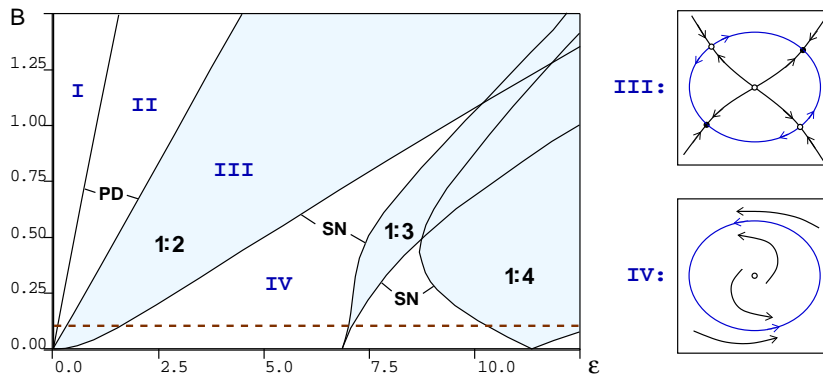
Figure 4: Simplified bifurcation diagram of system (15) in the (ε, B) parameter plane (left). In the shaded areas the tori are phase-locked. With the exception of the left boundary of the 1:2 phase-lock area, these areas are bounded by curves of saddle-node bifurcations. The figures to the right qualitatively sketch period-π stroboscopic maps in the regions C and D for small $B > 0$.

only for values of the ratio ω_2/ω_1 that satisfy certain number-theoretical conditions [7]. In particular, each point $(\varepsilon, 0)$ in the (ε, B)-parameter plane for which the ratio ω_2/ω_1 is rational, forms the tip of a so-called *Arnol'd tongue*. The bifurcation diagram of System (16)-(17) in the (ε, B) parameter plane is shown in Fig. 4 (left). We only show the Arnol'd tongues with $\omega_2/\omega_1 = 1/2, 1/3$, and $1/4$ (blue shaded areas), because these values give the widest Arnol'd tongues [10]. For sufficiently small forcing amplitude $B > 0$, the system's response inside the Arnol'd tongues is not quasi-periodic but sub-harmonic. (The dynamics inside an Arnol'd tongue for larger forcing amplitudes can be very complicated [22].)

Let us describe how the behaviour of the system varies with ε, assuming that $B > 0$ is relatively small, say, $B = 0.1$ (brown dashed line in Fig. 4). In region I only the periodic solution $\gamma_0 = (0, 0, 2t \bmod 2\pi)$ exists, and it is asymptotically stable. When crossing the boundary from region I to region II this solution loses stability in a period-doubling bifurcation. In region II the solution γ_0, now of saddle type, coexists with an attracting periodic solution. On the boundary from region II to region III, the solution γ_0 undergoes a further period-doubling bifurcation, thereby becoming a source. In region III the unstable solution γ_0, and the attracting periodic solution coexist with an additional periodic solution of saddle type. The saddle-node connection of the two periodic solutions that branched off γ_0 form a 1:2 phase-locked invariant torus; see also the sketched phase portrait of the stroboscopic map in Fig. 4 (top right). When crossing the boundary from region III to region IV, these two solutions disappear in a saddle-node bifurcation. Arbitrarily close to this boundary there exist attracting quasi-periodic invariant tori in region IV that coexist with the solution γ_0; see also the sketched phase portrait of the stroboscopic map in Fig. 4 (bottom right).

Since the derivation of our algorithm is only valid for tori that are densely covered by quasi-periodic solutions, we cannot expect that the algorithm works for parameter values inside the Arnol'd tongues. However, as we shall now see, the semi-discretisation method turns out to be rather robust.

4.1.2   Continuation of Quasi-Periodic Solutions

We computed the quasi-periodic solutions of system (15) for fixed $B = 0.1$ and varying $\varepsilon \in [0, 12]$ (brown dashed line in Fig. 4) using a real spectral system of order 5. The spectral system was discretised by central finite difference-quotients of order 4 on a regular mesh with 801 mesh-points. The integral phase condition (5) for periodic solutions was introduced to fix the unknown frequency ω_2 of the solution of the spectral system. Since simulations for $\varepsilon \approx 2$ indicate that the system's response is quasi-periodic and the invariant closed curve of the stroboscopic map almost circular, we used

$$y_0(\theta_2) = \begin{pmatrix} \sin(\theta_2) \\ \cos(\theta_2) \end{pmatrix}, \qquad y_k(\theta_2) = \begin{pmatrix} 0 \\ 0 \end{pmatrix}, \quad k = -5, \ldots, -1, 1, \ldots, 5,$$

and $\omega_2 = 0.95$ as an initial approximation for the solution at $\varepsilon = 2$. The discretised system was solved with Newton's method and the full branch of quasi-periodic solutions was computed for $\varepsilon \in [0, 12]$ using pseudo arc-length continuation with Newton's method as corrector. In either case, we stopped the Newton iteration when the Euclidean norm of the Newton correction became less that 10^{-8}, thus, the error made by Newton's method is negligible.

The convergence behaviour of our method depending on ε is illustrated in Fig. 5. The diagram on top shows the $\mathcal{L}_2$-norm of the coefficient functions for each Fourier-mode, which is indicated by the labels. On the left and the right ends of the diagram for $\varepsilon \leq 1.8$ and $\varepsilon \geq 10$, we observe two plateaus of slow convergence, which is due to the 1:2 and 1:4 sub-harmonic resonances which occur within wide Arnol'd tongues; compare with Fig. 4. For $1.8 < \varepsilon < 10$ the convergence seems exponential with the exception of isolated peaks. The estimated error of the finite-difference method, depicted in Fig. 5 (middle), shows a similar behaviour. The error is reasonably small, that is, ERR $\leq 10^{-2}$, except for a number of peaks that occur at the same parameter values as the peaks in the norms of the Fourier coefficients.

This behaviour is due to further p:q sub-harmonic responses. To see this, consider the diagram on the bottom of Fig. 5. It shows the ratio ω_2/ω_1 depending on ε, where $\omega_1 = 2$ is the forcing frequency and ω_2 is the frequency of the periodic solution of the spectral system. As explained in the previous section, a p:q sub-harmonic response (p:q phase-lock) occurs whenever this ratio is rational, that is, $\omega_2/\omega_1 = p/q$, where p and q are integers. The horizontal lines indicate the values p/q of sub-harmonic responses that visibly affect our computation. The plateaus and peaks in the norms of the Fourier coefficient functions and the estimated error of the finite-difference method occur exactly near parameter values for which the ω_2/ω_1-curve crosses these horizontal lines. In particular, we clearly observe a locking of the basic frequencies, namely, ω_2/ω_1 is (almost) constant within the 1:2 and 1:4 Arnol'd tongues.

The computed approximations of the tori for different parameter values are shown in Figs. 6 and 7 (right panels) together with steady solutions and corresponding phase portraits of the stroboscopic map obtained by simulation (left panels). The graphs are represented in an unwinded cylindrical phase-space, that is, the $(x, \dot{x})$ coordinates are interpreted as usual but the time coordinate has to be taken modulo π. This means that any solution curve leaving the time interval $[0, \pi]$ at one end, re-enters at exactly the same $(x, \dot{x})$ coordinates at the opposite end of the time interval. The tori in the right panels are recon-
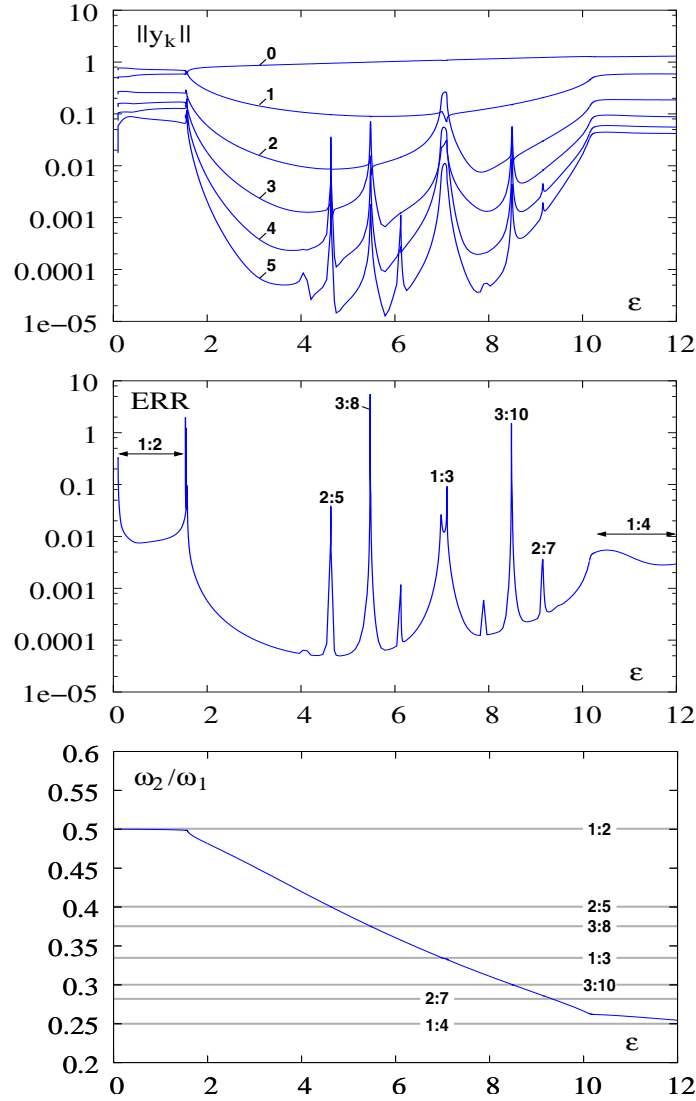
Figure 5: Norms of the Fourier coefficient functions (top), the estimated error of the periodic solution of the spectral system (middle) and the ratio ω_2/ω_1 (bottom) versus ε of the branch of quasi-periodic solutions of system (15) for $B = 0.1$.
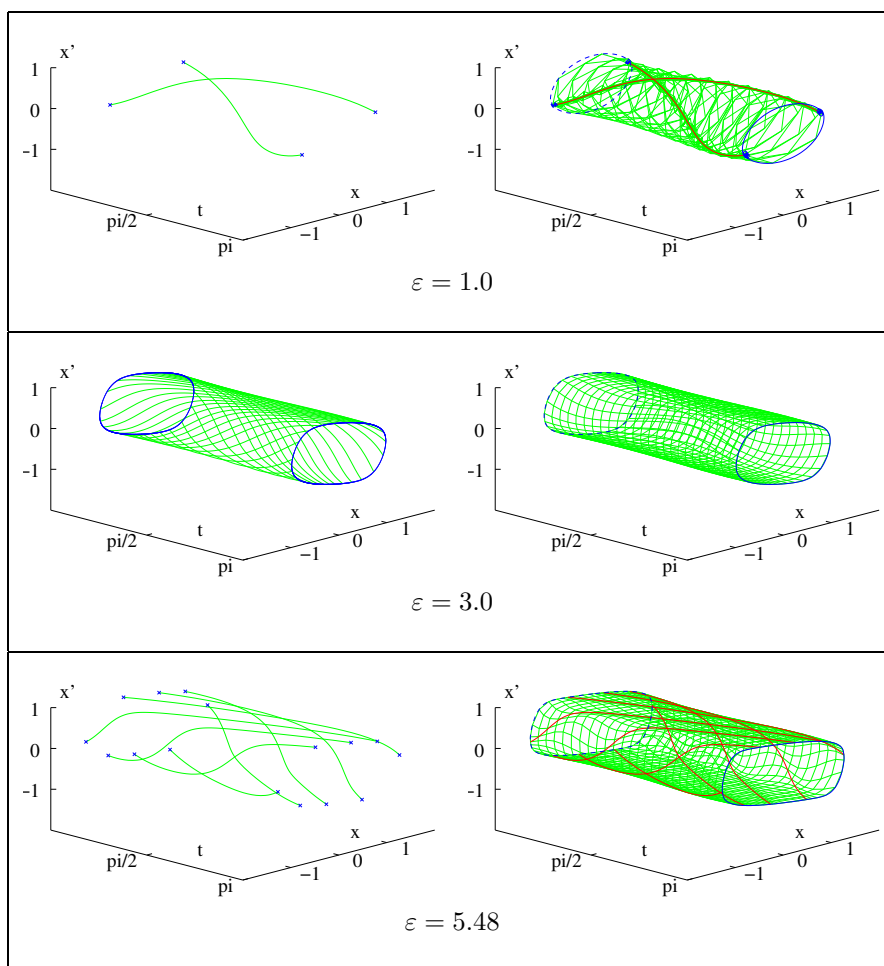
Figure 6: Steady solutions obtained by simulation (left) and approximations of the invariant tori (right) of system (15) for different parameter values; the sequence continues in Fig. 7. The blue crosses and curves in the figures on the left are periodic orbits or invariant curves the period-2π stroboscopic map at $t = 0$. The blue curves in the figures on the right are cross-sections of the tori at $\theta_1 = 0$; compare also with Fig. 3 (right). These curves are approximately invariant under the stroboscopic map.

Figure 7: Steady solutions (left) and approximations of the invariant tori (right) of system (15) for different parameter values; the sequence starts in Fig. 6.
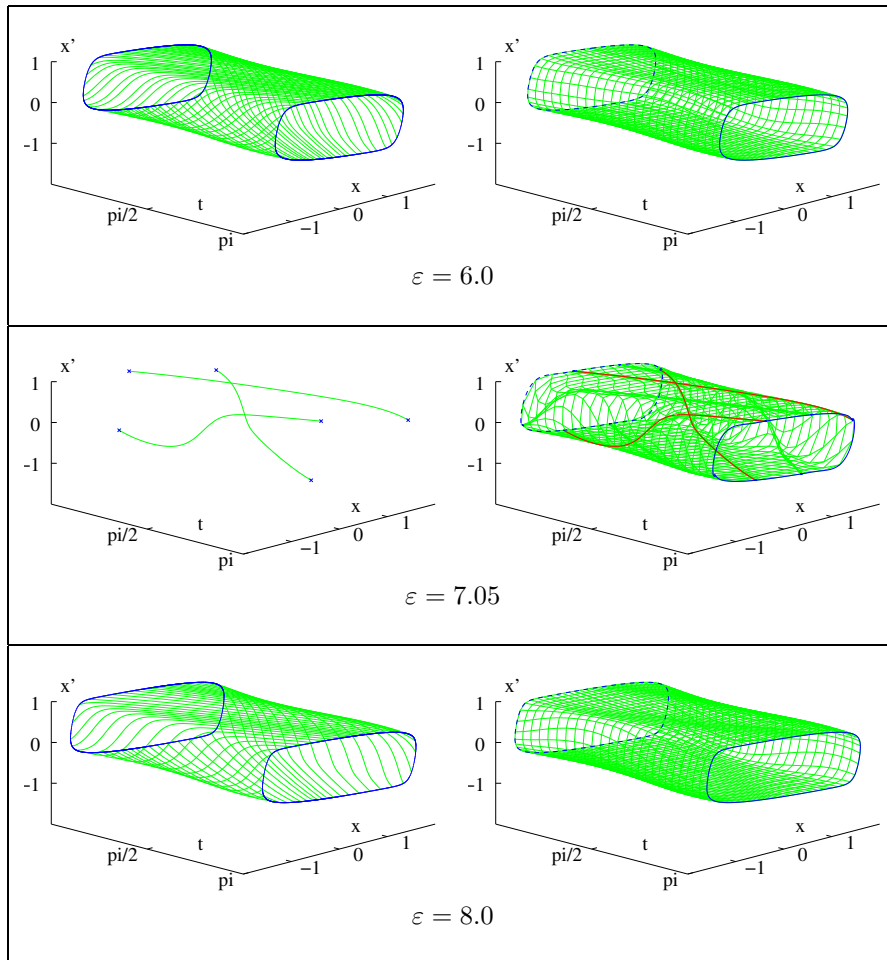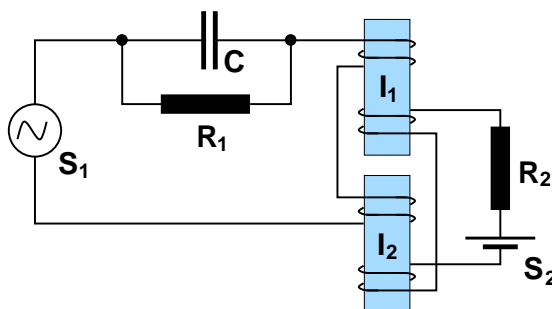
Figure 8: The resonant circuit with two saturable inductors (I_1 and I_2) described by system (19)-(22). In addition, the circuit contains an AC (S_1) and a DC (S_2) voltage source.

structions from the periodic solutions of the spectral system using the relation $u(\theta_1, \theta_2) = y_0(\theta_2) + \sum_{k=1}^{5} [\, y_k(\theta_2) \cos k\theta_1 + y_{-k}(\theta_2) \sin k\theta_1 \,]$. The cross-sections at $t = 0 \cong \pi$ are highlighted by the blue curves and are approximations to invariant closed curves of the period-π stroboscopic map even in the case of a sub-harmonic response. For $\varepsilon = 1.0$, $\varepsilon = 5.48$ and $\varepsilon = 7.05$ the attracting periodic solutions that reside on the tori are indicated by red curves. Here, we point out that the semi-discretisation method seems to be more robust when approximating phase-locked tori than the finite-difference methods discussed in [10]. The finite-difference methods described in [10] break down near the 1:2 and the 1:3 sub-harmonic resonances at $\varepsilon \approx 1.5$ and $\varepsilon \approx 7.05$, respectively. An approximation could only be computed for $\varepsilon \in [1.7, 7.0]$, while the semi-discretisation method is able to follow the full branch for $\varepsilon \in [0.3, 12]$ even though one has to exercise caution when interpreting the numerical results in the way shown above.

The response solutions are depicted by the green curves while the blue crosses or points represent iterates of the period-π stroboscopic map. These iterates densely fill an invariant closed curve, indicating that the oscillation is indeed quasi-periodic, in the middle panel of Fig. 6 ($\varepsilon = 3.0$) and the top and bottom panels of Fig. 7 ($\varepsilon = 6.0$ and $\varepsilon = 8.0$, respectively). In these figures only a short segment of the solution curve is shown to give an impression of the underlying torus. These tori become completely covered as one continues the simulations. In the top and bottom panels of Fig. 6 ($\varepsilon = 1.0$ and $\varepsilon = 5.48$, respectively) and the middle panel of Fig. 7 ($\varepsilon = 7.05$), the oscillation is not quasi-periodic but sub-harmonic and the underlying torus is phase-locked. For such parameter values attracting and unstable periodic solutions coexist on the torus, but only attracting solutions can be visualised by simulation; the frequencies for the shown examples are $\omega_2 = 1$, $\omega_2 = 3/4$ and $\omega_2 = 2/3$, respectively. The corresponding phase-locked tori in the right panels clearly display signs of slow convergence. The meshes appear to be non-smooth and seem to wind around the attracting periodic solution, particularly in the top right panel of Fig. 6.

4.2   A Resonant Circuit with Saturable Inductors

As our second example we consider a nonlinear electrical circuit given by Hayashi in [21]. The circuit is depicted in Fig. 8 and contains two loops. The first one is an oscillator built by the AC voltage source S_1, the capacitor C, the resistor R_1 and the two saturable inductors I_1 and I_2. The second loop superposes a DC bias and is formed by the DC voltage source S_2, the resistor R_2 and the inductors I_1 and I_2. The nonlinear characteristics of the iron cores of I_1 and I_2 are assumed to be cubic but hysteresis is ignored. This circuit can be described by the system of ODEs

$$\dot{x}_1 = x_2\,, \tag{19}$$

$$\dot{x}_2 = -k_1 x_2 - \frac{1}{8}(x_1^2 + 3x_3^2)x_1 + B\cos\theta\,, \tag{20}$$

$$\dot{x}_3 = -\frac{1}{8}k_2(3x_1^2 + x_3^2)x_3 + B_0\,, \tag{21}$$

$$\dot{\theta} = 1\,, \tag{22}$$

which has been extended, as before, to the cylindrical phase space $\mathbb{R}^3 \times S^1$ by adding equation (22). Here, $x \in \mathbb{R}^3$, $\theta \in S^1$ and $B_0, B, k_1, k_2 \in \mathbb{R}$ are free parameters. The variables x_i represent dimensionless quantities, which correspond to particular currents and voltages by means of a linear transformation. A detailed description of the derivation of these equations can be found in [21, 24] where this circuit was extensively analysed using simulation and averaging. For completeness and comparison we repeat some of these computations in Section 4.2.1.

In what follows we are interested in qualitative changes of the system's response as the damping parameter k_1 varies in the interval $k_1 \in [0.04, 0.16]$ and the other parameters, $B_0 = 0.03$, $B = 0.22$ and $k_2 = 0.05$, are fixed. Fig. 9 shows iterates of period-2π stroboscopic maps at $\theta = 0$ (blue) together with projections of steady solutions of System (19)-(22) into the (x_1, x_2, x_3)-coordinate system (green) for $k_1 = 0.09$, $k_1 = 0.07$, $k_1 = 0.05$ and $k_1 = 0.043$. At $k = 0.09$, the iterates of the stroboscopic map (blue dots, top left) densely fill an invariant closed curve, indicating that the response is quasi-periodic and, indeed, the steady solution (green dots) densely fills a 2-torus. A similar observation can be made for $k_1 = 0.07$ (top right). The blue dots densely fill an invariant closed curve, but here this curve performs a double loop. Apparently, for decreasing $k_1 \in [0.09, 0.07]$, a bifurcation similar to a period-doubling seems to occur in the stroboscopic map. As k_1 is reduced further (bottom left and right in Fig. 9), a cascade of such bifurcations seems to exist, leading to a strange attractor. As shown in the bottom right panel in Fig. 9, for $k_1 = 0.043$ the stroboscopic map no longer exhibits an invariant closed curve.

4.2.1   Analysis by Averaging

The qualitative behaviour of steady solutions of System (19)-(22) can be analysed accurately using the method of averaging [21, 24]. Suppose that responses

$k_1 = 0.09$

$k_1 = 0.07$

$k_1 = 0.05$

$k_1 = 0.043$
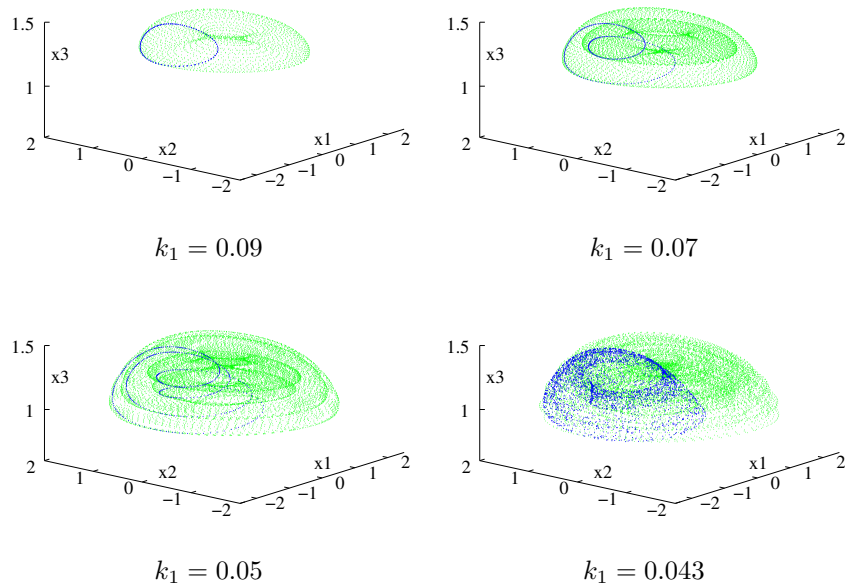
Figure 9: Steady solutions of system (19)-(22) obtained by simulation and projected onto the (x_1, x_2, x_3) coordinate system (green dots). The blue dots are iterates of the period-2π stroboscopic map at $\theta = 0$. For $k_1 = 0.09$, 0.07 and 0.05, these iterates densely fill invariant closed curves and the responses are quasi-periodic. For $k_1 = 0.043$ the stroboscopic map is no longer a curve and the system's response seems chaotic.

of (19)-(21) are approximately of the form

$$x_1(\theta) = y_1(\theta)\cos\theta + y_2(\theta)\sin\theta\,, \tag{23}$$
$$x_2(\theta) = -y_1(\theta)\sin\theta + y_2(\theta)\cos\theta\,, \tag{24}$$
$$x_3(\theta) = y_3(\theta)\,. \tag{25}$$

Here, we assume that the functions y_i are almost constant, that is, they are slowly varying amplitudes. Using the formulation (23)-(25) one can derive the averaged system

$$\dot{y}_1 = \frac{1}{2}(-k_1 y_1 - A y_2)\,, \tag{26}$$

$$\dot{y}_2 = \frac{1}{2}(A y_1 - k_1 y_2 + B)\,, \tag{27}$$

$$\dot{y}_3 = B_0 - \frac{1}{16}k_2(3r^2 + 2y_3^2)y_3\,, \tag{28}$$

$$\dot{\theta} = 1\,, \tag{29}$$

where the amplitudes $y \in \mathbb{R}^3$ and the phase $\theta \in S^1$ are now decoupled; see also [21, 24]. The terms A and r are defined as

$$A := 1 - \frac{3}{32}(r^2 + 4y_3^2)\,,$$
$$r^2 := y_1^2 + y_2^2\,.$$

Solutions of the averaged system (26)-(29) correspond to solutions of the full system (19)-(22) in the following sense; see also Theorem 1 and 2 in Section 2. If the amplitude equations (26)-(28) have an equilibrium point η, then, according to transformation (23)-(25), the full system has a periodic solution which is approximately given by

$$\begin{pmatrix} x_1(t) \\ x_2(t) \\ x_3(t) \\ \theta(t) \end{pmatrix} = \begin{pmatrix} \eta_1\cos t + \eta_2\sin t \\ -\eta_1\sin t + \eta_2\cos t \\ \eta_3 \\ t \bmod 2\pi \end{pmatrix}.$$

Similarly, a periodic solution of the amplitude equations gives rise to an invariant torus of the full system (19)-(22).

The bifurcation diagram of the amplitude equations (26)-(28) is shown in Fig. 10 and was computed using AUTO [12]. The black curve marked by label 1 is a branch of equilibrium solutions, which corresponds to periodic solutions of the full system (19)-(22). For decreasing $k_1 < 0.16$ these solutions lose stability in a Hopf bifurcation at $k_1 \approx 0.12$, and a branch of limit cycles emerges (blue curve, label 2). These limit cycles may correspond to quasi-periodic or sub-harmonic solutions of the full system (19)-(22), depending on the value of their frequency. At $k_1 \approx 0.08$ the limit cycles of the amplitude equations lose stability in a period-doubling bifurcation and a branch of period-doubled solutions emanates (green curve, label 3). Apparently, as k_1 decreases further, a cascade of period doublings occurs.

Since each periodic solution of the amplitude equations (26)-(28) corresponds to an invariant torus of the averaged system (26)-(29), and since in the averaged
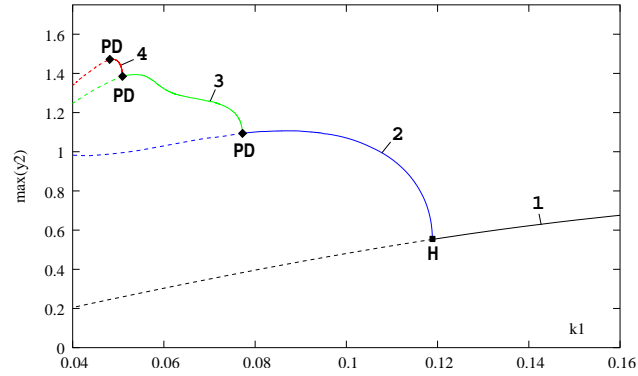
Figure 10: Bifurcation diagram of the amplitude equations (26)-(28).

$k_1 = 0.09$ $k_1 = 0.07$

$k_1 = 0.05$ $k_1 = 0.043$

Figure 11: Steady solutions of the averaged system (26)-(28) (blue curves) and the quasi-periodic solution approximated using (23)-(25) (green dots). For $k_1 = 0.09$, 0.07 and 0.05, the corresponding averaged system has limit cycle solutions. For $k_1 = 0.043$ the averaged equations give rise to a chaotic attractor.

Figure 12: Bifurcation diagram of the first-order spectral system of (19)-(22).

system amplitude and phase are decoupled, a period-doubling bifurcation of a periodic solution of the amplitude equations corresponds to a *torus-doubling bifurcati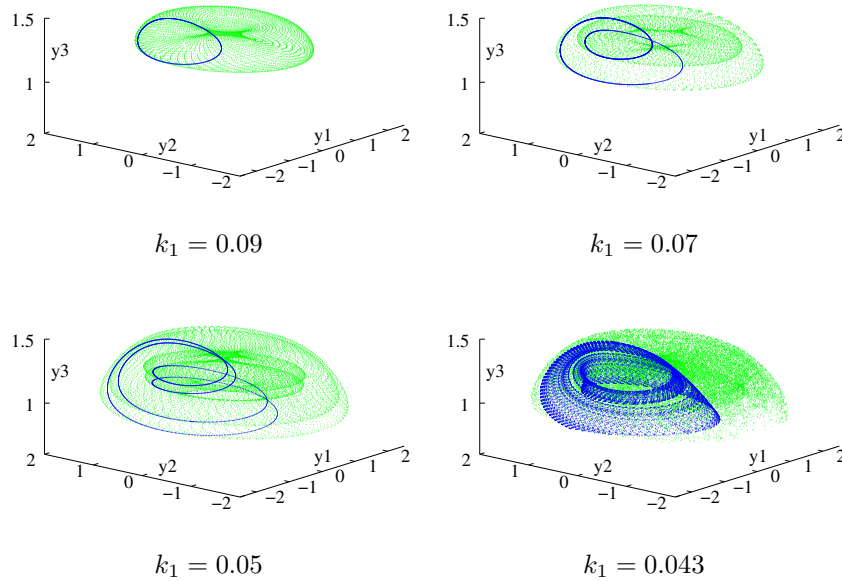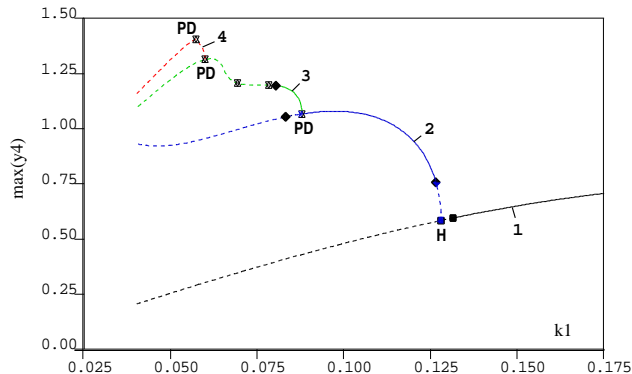on* of an invariant torus of the averaged system [25]. It can be shown that, under certain conditions, a torus-doubling bifurcation in the averaged system gives rise to a torus-doubling bifurcation in the full system. However, the bifurcation point is replaced by a small bifurcation interval and the cascade of period doublings in the averaged system becomes a finite sequence of bifurcations in the full system in which a smooth torus ceases to exist [25, 10, 26]. Fig. 11 shows steady states of the amplitude equation (blue curves) together with curves obtained by back substitution of these periodic solutions into (23)-(25) (green dots). Note that, according to (23)-(25), a periodic solution of the amplitude equation approximates an invariant closed curve of the period-2π stroboscopic map for $\theta = 0$ of the full system (19)-(22). Apparently, the solutions of the averaged system approximate the true behaviour of the full system with good accuracy; compare with Fig. 9.

4.2.2 Continuation of Quasi-Periodic Solutions

Our semi-discretisation method should mimic the computations for the averaged system while obtaining more accurate approximations of the quasi-periodic solutions of the full system (19)-(22). Unfortunately, we find that, although the computed approximations turn out to be very accurate, not all bifurcations in the spectral system correspond to bifurcations of the full system. For example, Fig. 12 shows the bifurcation diagram computed with AUTO [12] of the first-order real semi-discretised system, that is, we approximated solutions of the periodically forced sub-system (19)-(21) by

$$
\begin{pmatrix} x_1(t) \\ x_2(t) \\ x_3(t) \end{pmatrix} = \begin{pmatrix} y_1(t) + y_2(t)\sin t + y_3(t)\cos t \\ y_4(t) + y_5(t)\sin t + y_6(t)\cos t \\ y_7(t) + y_8(t)\sin t + y_9(t)\cos t \end{pmatrix},
$$

where the functions y_i are time-dependent amplitudes. The black curve marked by label 1 in Fig. 12 is the branch of equilibrium solutions of the spectral system, which correspond to periodic solutions of the full system (19)-(22). For decreasing k_1, not one but two consecutive Hopf bifurcations (a torus or Neimark-Sacker bifurcation of the periodic solution in the full system) occur at $k_1 \approx 0.131$ and
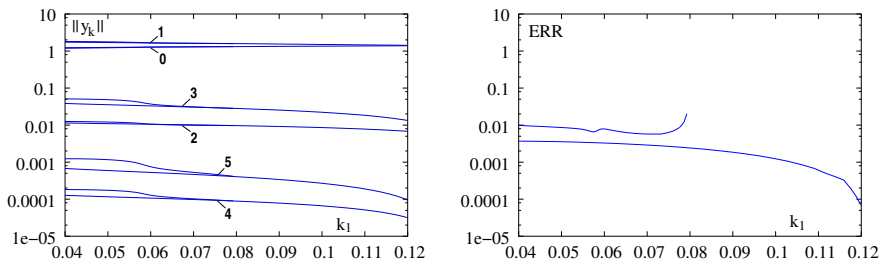
Figure 13: Norms of the Fourier coefficient functions (left) and the estimated error of the finite-difference method (right) for the branches of the primary and the period-doubled quasi-periodic solutions of system (19)-(22). The curves in the left panel are labelled according to the Fourier mode.

$k_1 \approx 0.128$. Indeed, as one increases the order of the spectral system, more and more such 'spurious bifurcations' occur and they accumulate near $k_1 \approx 0.1214$. Hence, one cannot 'naively' use standard bifurcation codes. In the example considered here, we chose the 'correct' solution path by visual investigation of the solutions. Subsequently, we followed the branch of periodic solutions (blue line, label 2) emerging from the Hopf bifurcation at $k_1 \approx 0.128$ whereby period-doubling and a number of spurious bifurcations are detected.

In a second computation, we continued the primary and the period-doubled quasi-periodic solution of system (19)-(22) using a semi-discretisation of order 5. The corresponding spectral system was discretised by finite differences of order 4 on regular meshes with 75 and 151 mesh-points for the primary and the period-doubled quasi-periodic solution, respectively. A phase condition was introduced to fix the unknown frequency ω_2 of periodic solutions of the spectral system. We obtained a start solution by minimising the residual $r(c, \omega_2) := \sum_{i=1}^{M}(x(t_i) - z(t_i))^2$, where $M \gg 2N + 1$ and $z(t) := \sum_{k,l} c_{kl} \exp(j(k + \omega_2 l)t)$ is a quasi-trigonometric polynomial, over a sufficiently large piece of a steady solution. This was done at $k_1 = 0.09$ for the primary and at $k_1 = 0.07$ for the period-doubled quasi-periodic solution.

The discretised system was solved with Newton's method and subsequently the full branches were computed for $k_1 \in [0.04, 0.12]$ using pseudo arc-length continuation with Newton's method as corrector. As before, we stop the Newton iteration when the Euclidean norm of the Newton correction is less than 10^{-8}. Fig. 13 illustrates the convergence behaviour of our algorithm depending on k_1. The diagram to the left shows the $\mathcal{L}_2$-norm of the coefficient functions for each Fourier mode, which is indicated by the labels. For all values of k_1 we observe exponential convergence and the coefficients of the even modes decrease faster than the odd ones. The diagram to the right shows the estimated error of the finite-difference discretisation, which is small for all values of k_1. We conclude that for all $k_1 \in [0.04, 0.12]$ the system's response is (almost) quasi-periodic.

Figs. 14 and 15 show projections onto the (x_1, x_2, x_3) coordinate system of the primary and the doubled tori, on which the quasi-periodic oscillations take place, for different values of k_1. These tori were reconstructed from the periodic solutions of the spectral system using the relation $u(\theta_1, \theta_2) = y_0(\theta_2) + \sum_{k=1}^{5}[y_k(\theta_2)\cos k\theta_1 + y_{-k}(\theta_2)\sin k\theta_1]$. The cross-sections at $\theta = 0$ are highlighted by the blue curves and are approximations to invariant closed curves of

$k_1 = 0.12$, $\omega_2 = 0.0935$, $T_2 = 67.182$ $k_1 = 0.10$, $\omega_2 = 0.0980$, $T_2 = 64.130$

$k_1 = 0.09$, $\omega_2 = 0.1023$, $T_2 = 61.444$ $k_1 = 0.04$, $\omega_2 = 0.1314$, $T_2 = 47.820$
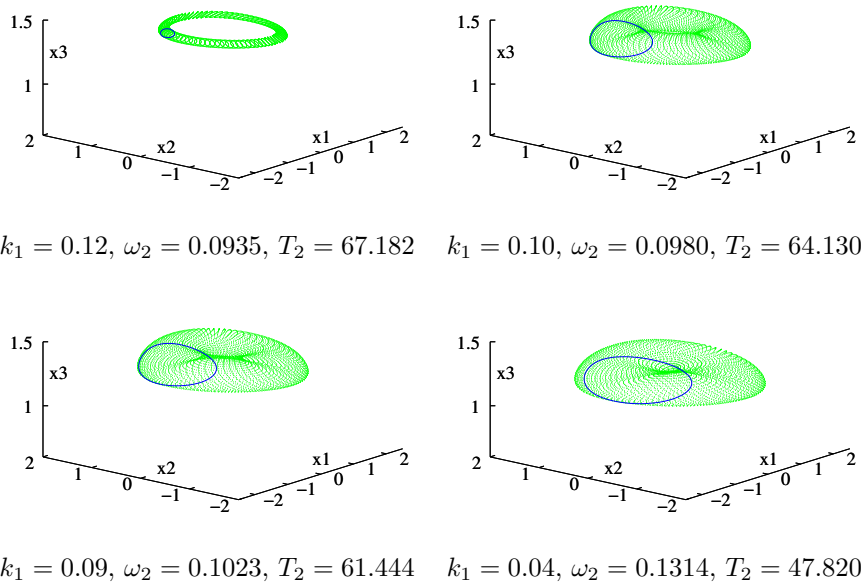
Figure 14: The primary quasi-periodic solution of system (19)-(22) projected onto the (x_1, x_2, x_3) coordinate system (green dots). The cross-sections for $\theta_1 = 0$ (blue) are approximate invariant curves of the period-2π stroboscopic map; compare the bottom left panel with the top left panel in Fig. 9. Note that the solution for $k_1 = 0.04$ is unstable and cannot be observed by simulation.

the period-2π stroboscopic map; compare Fig. 9 top left and right with Fig. 14 bottom left and Fig. 15 top right, respectively.

4.3   Performance of the Semi-Discretisation Method

If the right-hand side of the ODE (1) is a trigonometric polynomial with polynomial coefficients, $f(x, t) = p_0(x) + \sum_k [p_{2k-1}(x) \sin kt + p_{2k}(x) \cos kt]$, which is often the case in technical applications, then the method of semi-discretisation has the main advantage that the spectral system can be computed in closed symbolic form. Hence, the effort of actually generating the spectral system has to be made only once and we can expect that the semi-discretisation is superior to other methods, particularly if only a few modes (with variable coefficients) are required to obtain good approximations.

We implemented the semi-discretisation method as a symbolic algorithm within the two computer algebra systems Maple and MuPad and Table 1 shows the computation time depending on the order of the spectral system. For these computations we used MapleV R5.1 for Windows and MuPad 2.5.1 for LINUX on an Intel Pentium III CPU 800MHz. In both implementations, most of the time is spent on evaluating the function `combine`, which expands products of trigonometric functions according to the addition theorems.

Table 2 shows the computation times for the parametrically forced network for $\varepsilon = 2.0$ and Table 3 those for the resonant circuit with saturable inductors for $k_1 = 0.09$. These times were obtained on an Intel Xeon CPU 2.66GHz. In both tables we varied the order of the spectral system and the number of

$k_1 = 0.08,\ \omega_2 = 0.0533,\ T_2 = 117.98 \qquad k_1 = 0.07,\ \omega_2 = 0.0559,\ T_2 = 112.35$

$k_1 = 0.06,\ \omega_2 = 0.0625,\ T_2 = 100.50 \qquad k_1 = 0.04,\ \omega_2 = 0.0742,\ T_2 = 84.712$
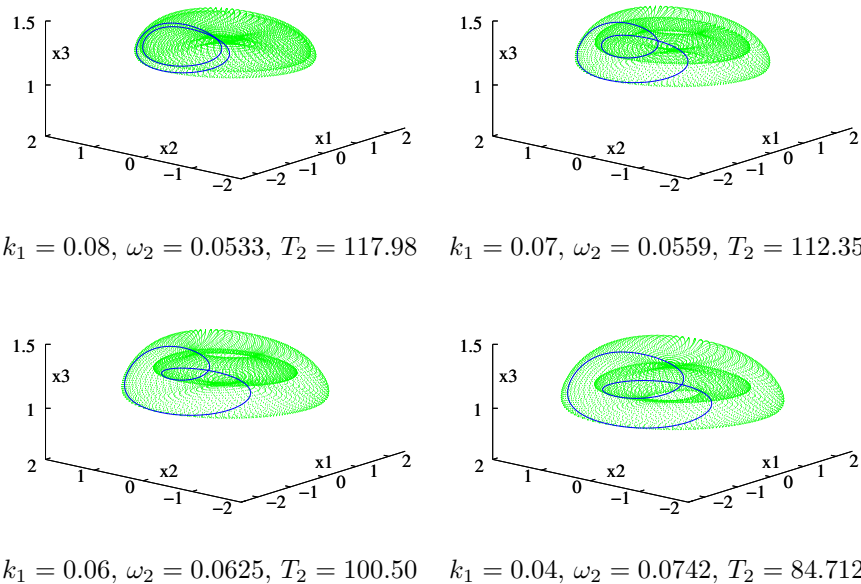
Figure 15: The period-doubled quasi-periodic solution of system (19)-(22) projected onto the (x_1, x_2, x_3) coordinate system (green dots). The cross-sections for $\theta_1 = 0$ (blue) are approximate invariant curves of the period-2π stroboscopic map; compare the top right panel with the top right panel in Fig. 9. Note that the solution for $k_1 = 0.04$ is unstable and cannot be observed by simulation.

	Parametrically Forced Network		System with Saturable Inductors	
Order	Maple	MuPad	Maple	MuPad
1	0.05	2	0.1	2
3	0.2	6	1.5	35
5	0.9	38	7	258
7	2.4	176	24	1296
9	5.3	623	67	—

Table 1: Computation times of the symbolic algorithm for generating spectral systems of increasing order (in seconds).

| Mesh- | Order=1 | | Order=3 | | Order=5 | | Order=7 | | Order=9 | |
points	eval.	tot.	eval.	tot.	eval.	tot.	eval.	tot.	eval.	tot.
51	0.0	0.1	0.1	0.2	0.2	0.5	0.3	0.9	0.6	1.5
75	0.0	0.1	0.1	0.3	0.3	0.9	0.5	1.3	0.8	2.0
101	0.0	0.1	0.2	0.5	0.5	1.1	0.7	1.8	1.1	2.7
125	0.1	0.2	0.2	0.6	0.5	1.3	0.8	2.1	1.5	3.5
151	0.1	0.2	0.3	0.8	0.6	1.6	1.0	2.6	1.7	4.2
175	0.1	0.2	0.3	0.8	0.8	1.9	1.3	3.2	2.0	4.9
201	0.1	0.2	0.4	1.0	0.9	2.2	1.4	3.6	2.3	5.6

Table 2: Computation times for computing the quasi-periodic solution of the parametrically forced network (15) with $\varepsilon = 2.0$ and $B = 0.1$ for different orders of the spectral system and different numbers of mesh-points used in the finite difference discretisation.

| Mesh- | Order=1 | | Order=3 | | Order=5 | | Order=7 | | Order=9 | |
points	eval.	tot.	eval.	tot.	eval.	tot.	eval.	tot.	eval.	tot.
51	0.1	0.2	0.2	0.5	0.5	1.1	1.0	2.1	2.1	3.7
75	0.1	0.2	0.2	0.7	0.6	1.6	1.4	3.0	3.1	5.6
101	0.1	0.3	0.4	1.3	0.9	2.6	2.0	4.6	4.2	8.0
125	0.1	0.3	0.4	1.5	1.2	3.3	2.4	5.7	5.3	10.1
151	0.1	0.3	0.6	2.0	1.4	4.3	2.9	7.3	6.1	12.3
175	0.2	0.5	0.6	2.2	1.7	5.9	3.3	9.5	7.0	15.5
201	0.2	0.5	0.7	2.5	1.9	6.6	3.8	10.9	8.2	17.9

Table 3: Computation times for computing the quasi-periodic solution of the circuit with saturable inductors (19)-(22) with $k_1 = 0.09$ for different orders of the spectral system and different numbers of mesh-points used in the finite difference discretisation.

mesh-points used to discretise the spectral system by finite differences of order 4. The tables show two columns for each order, indicating the time spent on evaluating the right-hand side of the spectral system and its Jacobian (eval.) and the total computation time for solving the discretised system (tot.). As one can see, the evaluation time becomes more and more dominant as the order of the spectral system grows. Thus, for high-order mode approximations it may become more efficient to evaluate the integrals in (14) numerically, which leads to the methods described in Section 5.

To give an impression of the efficiency of the semi-discretisation, we compare it with the finite-difference method described in [10]. First, we computed the quasi-periodic solution of the parametrically forced network for $\varepsilon = 2.0$ using the finite-difference method on a 41×101 mesh, which took 20 seconds. The same accuracy can be obtained using a spectral system of order 5 discretised by finite differences on 75 mesh points. The computation of the solution took 0.9 seconds, which gives a speed-up of 20. Secondly, we computed the quasi-periodic solution of the system with saturable inductors for $k_1 = 0.09$ with the finite-difference method on a 61×61 mesh, which took 13 seconds. A spectral system of order 5 discretised by finite differences on 75 mesh points provides the same accuracy and the solution was computed within 1.6 seconds, which again is much faster than the finite-difference method.

5   The Full-Discretisation Method

From now on, we consider the specific case where (1) is quasi-periodically forced ODE with $0 \leq m \leq p$ forcing frequencies. That is,

$$\dot{x} = f(x, \omega_1 t, \ldots, \omega_m t, \lambda), \qquad x \in \mathbb{R}^n, \ t, \lambda \in \mathbb{R}, \ n + m > p, \qquad (30)$$

where f is again 2π-periodic in each $\omega_i t$. This means that

$$f(x, \omega_1 t, \ldots, \omega_i t, \ldots \omega_m t, \lambda) = f(x, \omega_1 t, \ldots, \omega_i t + 2\pi, \ldots \omega_m t, \lambda), \quad i = 1, \ldots, m.$$

We assume that the right-hand side f is sufficiently smooth and use λ as a free parameter. This setting includes, in particular, autonomous systems ($m = 0$), periodically forced systems ($m = 1$), and so-called *response* systems ($m = p$). Note that, for $m \geq 1$, one can always rescale time such that $\omega_1 = 1$.

The full-discretisation method computes approximations of quasi-periodic solutions of system (30) using Fourier polynomials in *multiple* variables; a similar method already exists for maps [27, 28]. The result is a purely numerical algorithm that has a broader application area than the semi-discretisation method; see the example of two coupled Van der Pol oscillators in Section 6.3. In particular, it is the algorithm of choice if the integrals in (14) have to be evaluated numerically. The algorithm is derived in two steps: First, we apply Newton's method to the invariance equation (4) and obtain an extended linear PDE for the Newton correction. This linear PDE is then discretised using Fourier polynomials in p variables and the application of a Galerkin projection leads to a linear system, which has to be solved in each Newton step.

In what follows, we assume that (30) has a locally unique quasi-periodic solution $x(t) = u(\omega t)$ with the p-dimensional frequency base ω for some parameter value $\lambda = \lambda_0$. Since $x(t)$ is assumed to be a quasi-periodic solution of (30), its

associated torus function $u(\theta)$ is a solution of the invariance equation (4)-(5). Note that, due to the quasi-periodic forcing, we can omit the first m phase conditions in (5). Let us assume that we know approximations $u^{(\nu)}$ and $\omega^{(\nu)}$ of the solution of the invariance condition (4) and the basic frequencies, respectively. Our goal is to improve these approximations by the Newton-Raphson method for functions. We denote the residual of our approximate solution by

$$g(u^{(\nu)}, \omega^{(\nu)}, \theta) := f(u^{(\nu)}(\theta), \theta) - \sum_{i=1}^{p} \omega_i^{(\nu)} \frac{\partial u^{(\nu)}(\theta)}{\partial \theta_i},$$

and the Jacobian of f by

$$A(u^{(\nu)}, \theta) := f_x(u^{(\nu)}(\theta), \theta).$$

Here, we omitted $\lambda = \lambda_0$ in the argument of f and related functions. The Newton-Raphson method then reads

$$\left[A(u^{(\nu)}, \theta) - \sum_{i=1}^{p} \omega_i^{(\nu)} \frac{\partial}{\partial \theta_i} \right] v^{(\nu)} - \sum_{i=m+1}^{p} \eta_i^{(\nu)} \frac{\partial u^{(\nu)}}{\partial \theta_i} = -g(u^{(\nu)}, \omega^{(\nu)}, \theta), \quad (31)$$

$$\left\langle \frac{\partial u^{(\nu)}}{\partial \theta_i}, v^{(\nu)} \right\rangle_{\mathcal{L}_2^n} = 0, \qquad i = m+1, \ldots, p, \quad (32)$$

$$\begin{pmatrix} u^{(\nu+1)} \\ \omega^{(\nu+1)} \end{pmatrix} = \begin{pmatrix} u^{(\nu)} \\ \omega^{(\nu)} \end{pmatrix} + \begin{pmatrix} v^{(\nu)} \\ \eta^{(\nu)} \end{pmatrix}. \quad (33)$$

Equations (31)-(32) form an extended linear PDE for the Newton corrections $v^{(\nu)}$ and $\eta^{(\nu)} = (0, \ldots, 0, \eta_{m+1}^{(\nu)}, \ldots, \eta_p^{(\nu)})$, while Equation (33) is the actual correction step. Since $\langle \partial u^{(\nu)} / \partial \theta_i, u^{(\nu)} \rangle_{\mathcal{L}_2^n} = 0$ holds for all differentiable torus functions $u^{(\nu)}$ and all $i = 1, \ldots, p$, we simplify Equation (32) by setting $\tilde{u} = u^{(\nu)}$. Note that this must be done in each Newton step.

We approximate the solution of (31)-(32) by multi-dimensional Fourier polynomials in the p angular variables $\theta_1, \ldots, \theta_p$, which leads to a finite-dimensional linear system for the unknown Fourier-coefficient vectors. Let $\mathbb{I}_N := \{-N_1, \ldots, N_1\} \times \cdots \times \{-N_p, \ldots, N_p\} \subset \mathbb{Z}^p$ be a finite set of p-dimensional multi-indices and $\mathcal{H}_N^n \subset \mathcal{L}_2^n$ be the linear subspace spanned by the first $k \in \mathbb{I}_N$ Fourier monomials $e^{j\langle k, \theta \rangle}$ with n-dimensional complex Fourier-coefficient vectors as defined by (3), that is, $\mathcal{H}_N^n := [\text{span}\{e^{j\langle k, \theta \rangle}, \ k \in \mathbb{I}_N\}]^n$. Within this setting, the projection or truncation operator $P_N : \mathcal{L}_2^n \to \mathcal{H}_N^n$ is defined by truncating the Fourier series (3) to the first $k \in \mathbb{I}_N$ Fourier modes. In other words, a torus function $u : \mathbb{T}^p \to \mathbb{R}^n$ is mapped to its Fourier polynomial $u_N(\theta) := (P_N u)(\theta) := \sum_{k \in \mathbb{I}_N} u_k \, e^{j\langle k, \theta \rangle}$. The linear subspace $\mathcal{H}_N^{n \times n} \subset \mathcal{L}_2^{n \times n}$ of matrix functions $A : \mathbb{T}^p \to \mathbb{R}^{n \times n}$ is defined in a similar way.

If we denote the projections of $u^{(\nu)}$ and $v^{(\nu)}$ onto $\mathcal{H}_N^n$ by $u_N^{(\nu)}$ and $v_N^{(\nu)}$, then Galerkin's method applied to (31)-(32) can be written as

$$P_N \left(\left[A(u_N^{(\nu)}, \theta) - \sum_{i=1}^{p} \omega_i^{(\nu)} \frac{\partial}{\partial \theta_i} \right] v_N^{(\nu)} - \sum_{i=m+1}^{p} \eta_i^{(\nu)} \frac{\partial u_N^{(\nu)}}{\partial \theta_i} \right) =$$
$$-P_N \, g(u_N^{(\nu)}, \omega^{(\nu)}, \theta), \quad (34)$$

$$\left\langle \frac{\partial u_N^{(\nu)}}{\partial \theta_i} \, , \, v_N^{(\nu)} \right\rangle_{\mathcal{L}_2^n} \quad = \quad 0, \qquad m + 1 \le i \le p. \tag{35}$$

That is, we require Equations (31)-(32) to hold on the finite-dimensional subspace $\mathcal{H}_N^n$ only. In particular, Equation (34) is satisfied if and only if the Fourier coefficients of the left- and right-hand side are equal. System (34)-(35) can be rewritten as a linear equation system by computing these Fourier coefficients explicitly:

$$\sum_{l \in \mathbb{I}_N} A_{k-l}^{(\nu)} v_l^{(\nu)} - j \left(\sum_{i=1}^p \omega_i^{(\nu)} k_i \right) v_k^{(\nu)} - j \left(\sum_{i=m+1}^p \eta_i^{(\nu)} k_i \right) u_k^{(\nu)} =$$
$$-g_k^{(\nu)}, \quad k \in \mathbb{I}_N, \tag{36}$$

$$\sum_{k \in \mathbb{I}_N} k_i \langle u_k^{(\nu)} \, , \, v_k^{(\nu)} \rangle_{\mathbb{C}^n} \quad = \quad 0, \qquad m + 1 \le i \le p, \tag{37}$$

where the term $\sum_{l \in \mathbb{I}_N} A_{k-l}^{(\nu)} v_l^{(\nu)}$ was computed using the convolution rule. Here, $A_k^{(\nu)}$ denotes the kth Fourier-coefficient matrix of $A(u_N^{(\nu)}, \theta)$, and $g_k^{(\nu)}$ the kth Fourier-coefficient vector of the residual $g(u_N^{(\nu)}, \omega^{(\nu)}, \theta)$.

System (36)-(37) is an $(r + s)$-dimensional dense system of complex linear equations for the Fourier-coefficient vectors $v_k^{(\nu)}$, $k \in \mathbb{I}_N$, and the real numbers $\eta_{m+1}^{(\nu)}, \dots, \eta_p^{(\nu)}$, with $r = n(2N_1 + 1) \cdots (2N_p + 1)$ and $s = p - m$. This system is square and can be solved, for example, by Gaussian elimination. If we omit the $p - m$ phase conditions (37), we obtain a rectangular system with r equations and $r + s$ unknowns of the form

$$Lv = g, \qquad v \in \mathbb{C}^{r+s}, \ \ g \in \mathbb{C}^r, \ \ L \in \mathbb{C}^{r \times (r+s)},$$

where we collected $v_k^{(\nu)}$ and $\eta_{m+1}^{(\nu)}, \dots, \eta_p^{(\nu)}$ in the vector v and $-g_k^{(\nu)}$ in the vector g using, for example, lexicographical ordering of the multi-indices $k \in \mathbb{I}_N$. The chosen ordering together with (36) uniquely defines the matrix L. The solution of this linear equation system can be computed using the Moore-Penrose pseudo-inverse L^+, which, assuming that the full-rank condition $\text{rank}(L) = r$ holds, is defined as

$$L^+ = L^*(LL^*)^{-1}$$

where L^* is the (complex) transpose of L. This technique is implemented as follows. First, we construct the regular matrix LL^*. Then, we solve the linear system $(LL^*)w = g$ for $w \in \mathbb{C}^r$. Finally, we compute the solution $v = L^*w$. This procedure proved to be reliable independent of the number of forcing and basic frequencies. Moreover, for large r and small s, our MATLAB implementation of this algorithm turned out to be more efficient than the QR-factorisation used by MATLAB's \-operator. However, if the matrix L is ill-conditioned one has to apply the more stable QR factorisation.

We implemented the full-discretisation method in MATLAB V6.5 R13 for autonomous or periodically forced periodic solutions ($p = 1$ and $m = 0, 1$), and for autonomous, periodically forced, or quasi-periodically forced quasi-periodic solutions with two basic frequencies ($p = 2$ and $m = 0, 1, 2$) using the pseudo-inverse algorithm described above. The Fourier-coefficients are computed by

the fast Fourier transform (MATLAB functions `fft` and `fft2`). To estimate the error of a numerical solution (u_N, ω) we compute the maximum residual norm $\|g(u_N(\theta), \omega, \theta)\|$ over a sufficiently large set of θ-values that are different from the sample points used for the fast Fourier transform. Note that the error estimated by the residual is not quantitatively comparable with the error estimated as the difference of solutions of different approximation orders as used for the semi-discretisation method. The current implementation of the algorithm is not adaptive but the order of the Fourier polynomial is heuristically adjusted during parameter continuation.

Remark. If the system is a response system, that is $m = p$, then the full-discretisation method is identical to the Harmonic Balance Method [15] when $p = 1$, and the Spectral Balance Method [15] when $p > 1$.

6 Examples

We demonstrate the performance of the full-discretisation method with three examples. Sections 6.1 and 6.2 discuss the respective examples of the parametrically forced network and the resonant circuit with saturable inductors that were analysed in Section 4 using the semi-discretisation method. Where appropriate, we choose the same parameter values and ranges. Both examples show that the full-discretisation method is as robust and reliable as the semi-discretisation method. In Section 6.3 we compute quasi-periodic solutions of two coupled Van der Pol oscillators, a system for which the semi-discretisation method is not applicable. This system is also used as a test example for a different Fourier-Galerkin method in [29].

6.1 The Parametrically Forced Network Revisited

We recomputed the quasi-periodic solutions of system (15) for fixed $B = 0.1$ and varying $\varepsilon \in [0, 12]$ (brown dashed line in Fig. 4) using the full-discretisation method. As a start solution for $\varepsilon = 2.0$ we chose the Fourier series of the function $(\cos \theta_2, \sin \theta_2)$ together with the initial guess $\omega_2 = 0.98$ for the unknown second basic frequency. We compute the branch of quasi-periodic solutions for $\varepsilon \in [0, 12]$ using pseudo arc-length continuation with the full-discretisation method as corrector. The Newton iterations stop when the Euclidean norm of the Newton correction falls below 10^{-6}.

The convergence behaviour of the method depending on ε is illustrated in Fig. 16; compare Fig. 5. For comparison with the semi-discretisation method, we collected the terms $u_N(\theta) = \sum_{k \in \mathbb{I}_N} u_k e^{j\langle k, \theta \rangle}$ in θ_1 as described in Section 3.1 and computed the norms of the coefficient functions $y_k(\theta_2) = \sum_{l=-N_1}^{N_1} u_{kl} e^{jl\theta_2}$; the latter are shown for $k = 0, \dots, 5$ in the top panel of Fig. 16. The middle panel shows the estimated residual of the approximate solution and the bottom panel the ratio $\omega_2/\omega_1 = \omega_2/2$ as a function of ε. The qualitative behaviour is virtually the same as for the semi-discretisation method. For $\varepsilon \leq 1.8$ and $\varepsilon \geq 10$ we observe plateaus of slow (or no) convergence and for $1.8 < \varepsilon < 10$ the convergence seems exponential with the exception of isolated peaks that correspond to some sub-harmonic resonances as indicated.

Figures 17 and 18 show the computed approximations of invariant tori and contour plots of the norms of the corresponding Fourier-coefficient vectors for
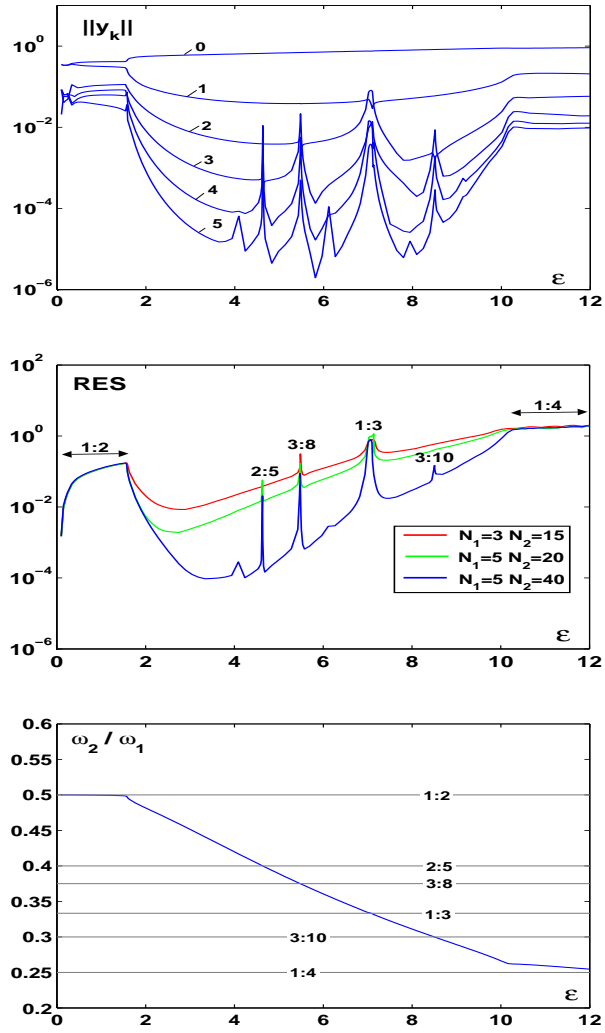
Figure 16: Norms of the Fourier coefficient functions for $k = 0, \ldots, 5$ (top), the estimated residual (middle) and the ratio ω_2/ω_1 (bottom) versus ε on the branch of quasi-periodic solutions of the parametrically forced network (15) for $B = 0.1$.
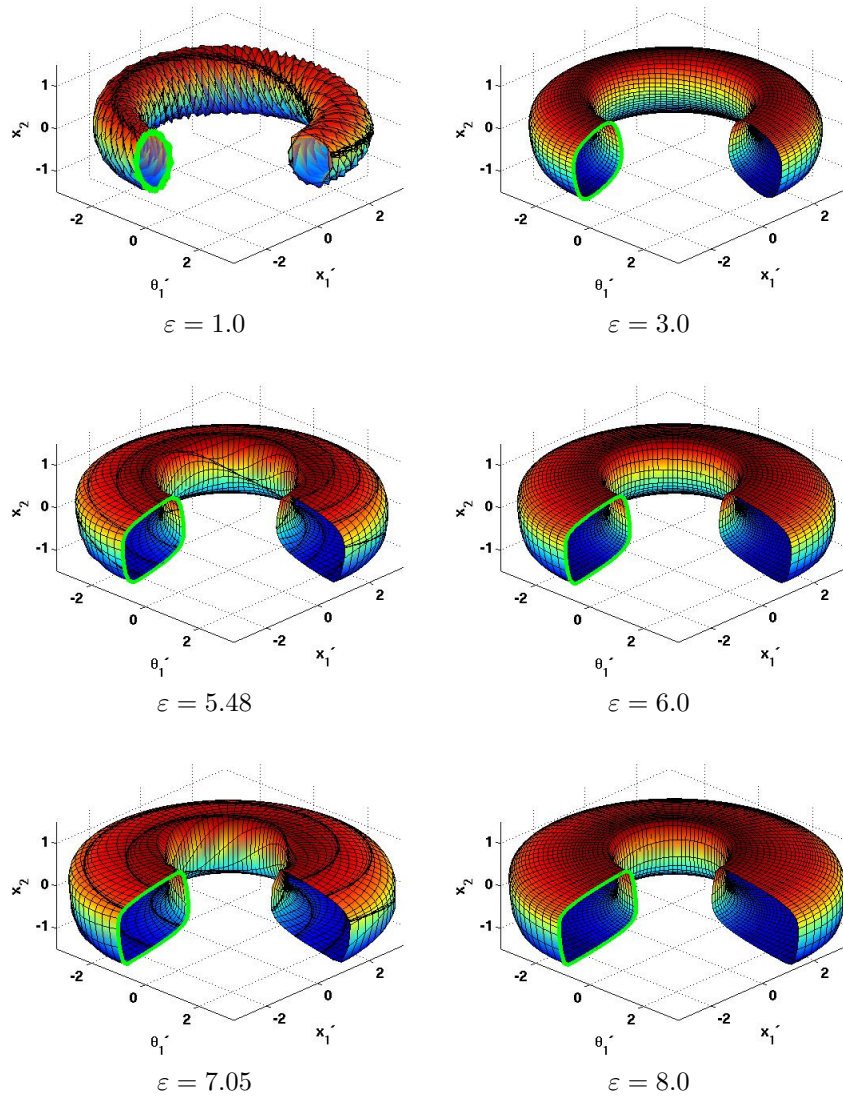
Figure 17: Approximations of the invariant tori of the parametrically forced network (15) for increasing values of ε; compare also Figs. 6 and 7. The green curves are cross-sections of the tori for $\theta_1 = 0$ and are approximations of the invariant curves of the stroboscopic map at $t = 0$; see also Fig. 18 .

$\varepsilon = 1.0$

$\varepsilon = 3.0$

$\varepsilon = 5.48$

$\varepsilon = 6.0$
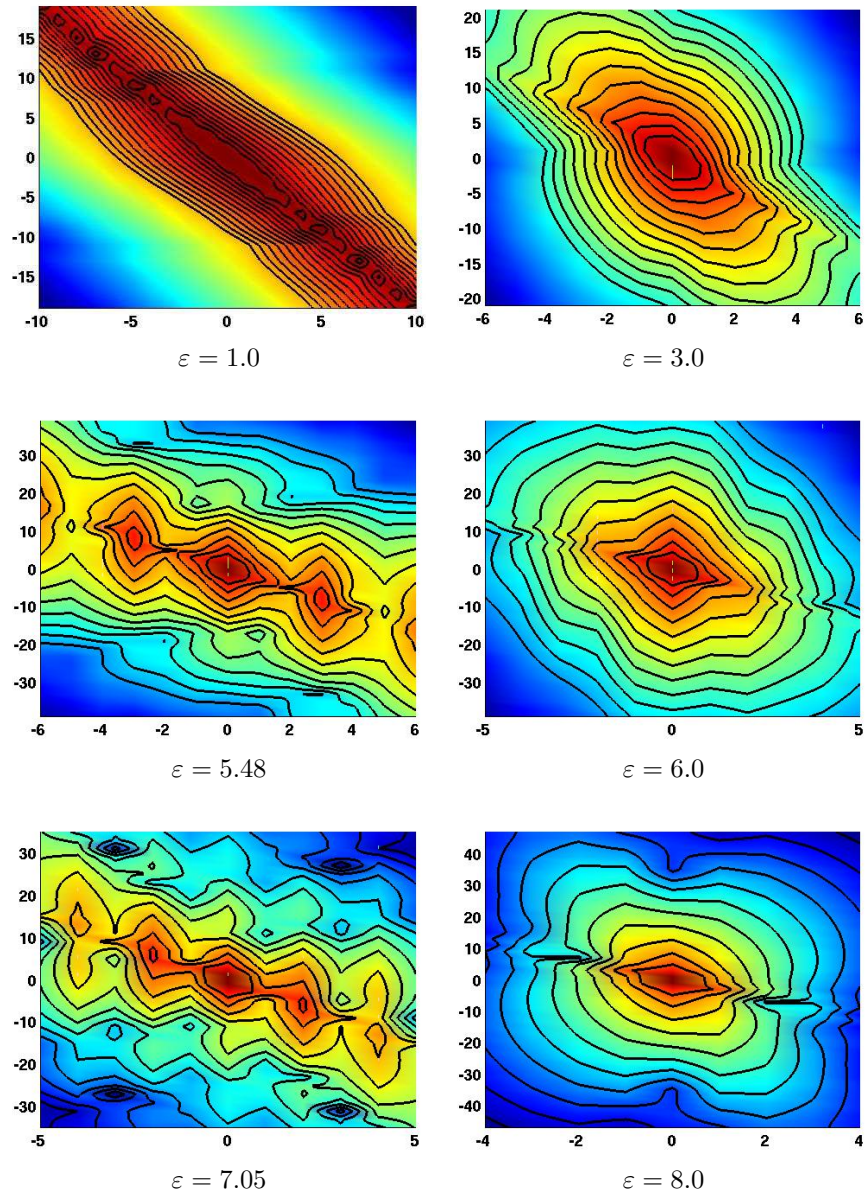
$\varepsilon = 7.05$

$\varepsilon = 8.0$

Figure 18: Contour plots of the norms of the Fourier-coefficient vectors for the invariant tori in Fig. 17. The contours are coloured on a logarithmic scale illustrating the decay of the coefficients.

varying values of ε, respectively. The tori in Fig. 17 were embedded into $\mathbb{R}^3$ by the change of coordinates

$$\theta_1' = r + x \cos \theta_1, \qquad x_1' = r + x \sin \theta_1, \qquad x_2 = \dot{x},$$

where the torus radius r is chosen large enough such that the torus has a hole (we used $r = 3$). Figure 17 only shows the parts of the tori with $0 \leq \theta_1 \leq \frac{3}{2}\pi$ with the cross-section for $\theta_1 = 0$ highlighted in green. Figure 18 shows the contour plots of the norms of the Fourier-coefficient vectors for the invariant tori in Fig. 17. The contour plots are coloured on a logarithmic scale and we omitted all coefficients that are close to zero. As with the semi-discretisation method, the full-discretisation method converges quickly for parameter values where the solution is quasi-periodic. For $\varepsilon = 3.0$, $\varepsilon = 6.0$ and $\varepsilon = 8.0$ this is clearly indicated by the exponential decay of the Fourier coefficients as shown in the right panels of Fig. 18. That is, we observe an 'island structure' which indicates a decay of the Fourier coefficients in all directions, and the black level-curves are approximately equally spaced. In contrast, we observe a band-like structure in the contour plots for $\varepsilon = 1.0$, $\varepsilon = 5.48$ and $\varepsilon = 7.05$, where the solution is not quasi-periodic but 1:2, 3:8 and 1:3 sub-harmonic, respectively. Here, the Fourier coefficients do not decay in the direction $qN_1 \approx pN_2$, with p and q determined by the type p:q of the sub-harmonic resonance; see the left panels in Fig. 18. For these parameter values, the approximations of the tori seem non-smooth, that is, the displayed tori are rippled, which is particularly apparent for $\varepsilon = 1.0$; see the left panels in Fig. 17. In the panels for $\varepsilon = 5.48$ and $\varepsilon = 7.05$ the mesh is overlapping itself at the darker lines. The value of the residual, as depicted in the middle panel of Fig. 16, clearly indicates for which parameter values the solution can be trusted. We point out that, like the semi-discretisation method, the full-discretisation method seems more robust when approximating phase-locked tori than the finite-difference method discussed in [10].

6.2 The Resonant Circuit with Saturable Inductors Revisited

We recomputed the primary and period-doubled quasi-periodic solutions of system (19)-(22) for $k_1 \in [0.04, 0.12]$ using the full-discretisation method. We obtained an initial choice of Fourier-coefficient vectors and the second basic frequency ω_2 in the same way as in Section 4.2 by approximating a sufficiently large piece of a steady solution with quasi-trigonometric polynomials. The k_1-dependent branches were computed using pseudo arc-length continuation with the full-discretisation method as corrector. The Newton iteration is again stopped when the Euclidean norm of the Newton correction is less than 10^{-8}. Figure 19 illustrates how the convergence behaviour of our algorithm depends on k_1. The diagram shows the estimated residual of the approximate solutions. For all values of k_1 we observe exponential convergence.

The periodic solution and the primary and period-doubled quasi-periodic tori for $k_1 = 0.074$ are shown together in Fig. 20 (left) to give an impression how these solutions coexist in phase space. Note, that the full-discretisation method is also not influenced by the stability type of the approximated quasi-periodic torus. Consequently, our continuation algorithm has no problem stepping over
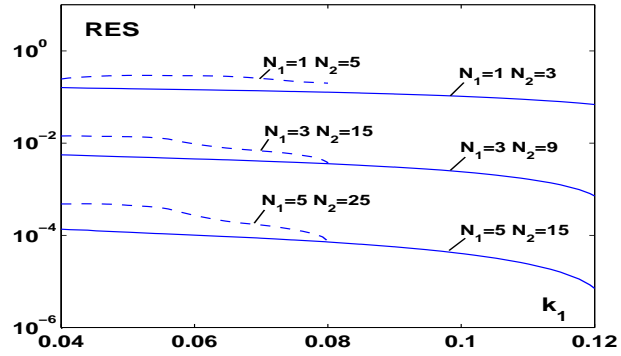
Figure 19: The estimated residuals for the primary (solid) and period-doubled (dashed) quasi-periodic solution branches of the system with saturable inductors (19)-(22) for different discretisation orders $N_1 \times N_2$ as indicated by the labels.
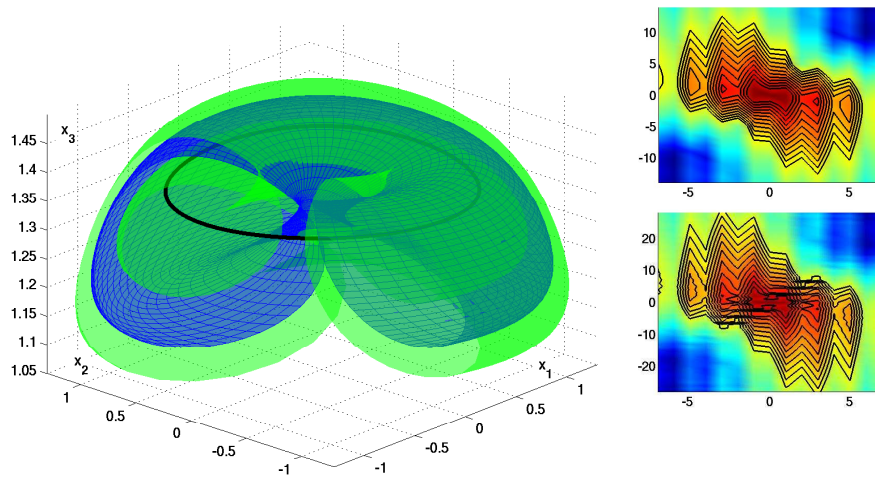
Figure 20: The periodic solution (black), the primary quasi-periodic torus (blue) and the period-doubled quasi-periodic torus (green) of the system with saturable inductors (19)-(22) for $k_1 = 0.074$. The periodic solution and the primary quasi-periodic torus are unstable, and the period-doubled quasi-periodic torus is attracting. The right column illustrates the decay of the Fourier coefficients for the primary (top) and the period-doubled (bottom) torus.

regions where the tori change their stability type, in this example from attracting to saddle-type. The right column in Fig. 20 illustrates the decay of the Fourier coefficients for the primary (top) and the period-doubled (bottom) tori. The number of Fourier modes used for the doubled torus in the θ_2-direction is about twice that for the primary torus.

6.3 Two Coupled Van der Pol Oscillators

In our last example we compute and continue quasi-periodic solutions of the autonomous system of two coupled Van der Pol oscillators

$$\ddot{x} - \varepsilon(1 - x^2)\dot{x} + \gamma_1^2 x = -\delta(ay^2 + bx^2y^2)\dot{x}, \tag{38}$$

$$\ddot{y} - \varepsilon(1 - y^2)\dot{y} + \gamma_2^2 y = -\delta(\alpha x^2)\dot{y}. \tag{39}$$

The parameter ε controls the nonlinear damping, γ_1 and γ_2 determine the internal frequencies for $\varepsilon = \delta = 0$, and δ is a measure of the mutual interaction within the oscillators which is also influenced by the choice of a, b and α. Invariant tori of system (38)-(39) were previously analysed with a different Fourier method in [13, 29]; see also [30]. The main difference with the full-discretisation method is that the algorithms proposed in [13, 29, 30] require an a-priory transformation into torus (radius-angle, action-angle) coordinates; see below for more details. This is a major restriction to the applicability of these algorithms, because such a transformation is only possible in special cases and seems already problematic for this example. Our approach to overcomes this difficulty.

6.3.1 Preliminary Analysis

The existence of invariant tori on which quasi-periodic and phase-locked oscillations take place can qualitatively be shown as follows. Consider the decoupled case for $\delta = 0$. If also $\varepsilon = 0$ then we have a system of two decoupled harmonic oscillators with internal frequencies γ_1 and γ_2, respectively. For $\varepsilon > 0$ each of the oscillators has a limit cycle with internal frequencies ω_1 and ω_2 that converge to γ_1 and γ_2 as ε approaches zero. We conclude that for $\delta = 0$ and $\varepsilon > 0$ System (38)-(39) has a normally attracting invariant torus $T_\varepsilon = \xi_\varepsilon \times \eta_\varepsilon$ that is the product of the limit cycles ξ_ε for the first and η_ε for the second oscillator with internal frequencies ω_1 and ω_2, respectively. All oscillations on T_ε are quasi-periodic if the ratio ω_1/ω_2 is irrational and periodic otherwise. If we now enable a coupling $\delta > 0$ the tori T_ε will survive as smooth tori for sufficiently small values of δ due to normal attraction, which is a special case of normal hyperbolicity [23]. On the other hand, as discussed in Section 1 the dynamics on the tori may change.

The analysis carried out above suggests that for small δ the tori may be parametrised in polar coordinates, using the limit cycles ξ_ε and η_ε:

$$
\begin{array}{llll}
\xi_\varepsilon & : & x = r_1(\theta_1)\cos\theta_1 & \dot{x} = -r_1(\theta_1)\sin\theta_1, \\
\eta_\varepsilon & : & y = r_2(\theta_2)\cos\theta_2 & \dot{y} = -r_2(\theta_2)\sin\theta_2.
\end{array}
$$

This coordinate transformation leads to an ODE in the torus coordinates $(r_1, \theta_1, r_2, \theta_2)$, which can be used to derive a PDE for the invariant torus as a function of the angular variables (θ_1, θ_2). This idea was followed, in principle, in [13, 29, 30].
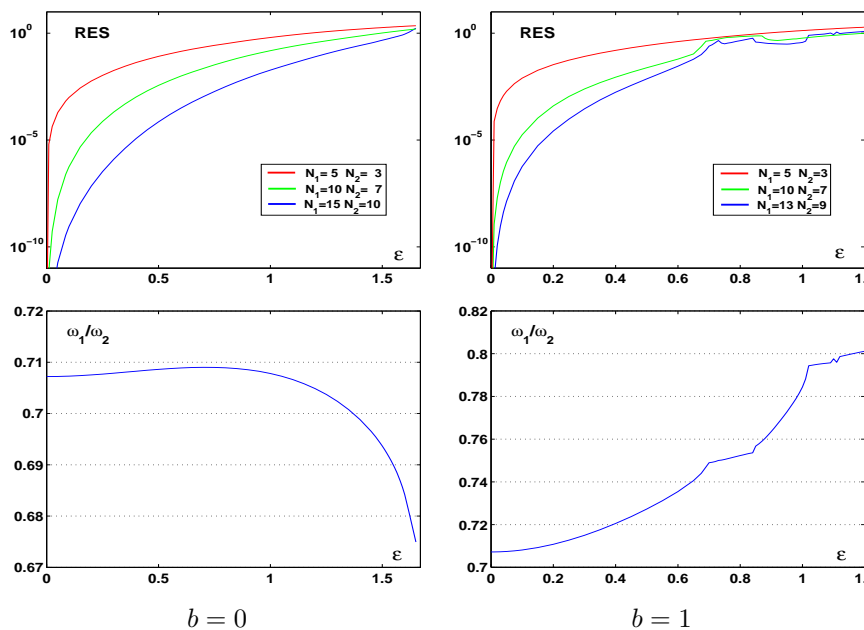
$b = 0$ $b = 1$

Figure 21: Norm of the residual (top) and the ratio ω_2/ω_1 (bottom) versus ε for the quasi-periodic solution branches of system (38)-(39).

6.3.2 Continuation of Quasi-Periodic Solutions

For our computations we used the same parameter values as in [13, 29], that is, $\gamma_1 = 1$, $\gamma_2 = \sqrt{2}$, $a = 0.2$, $\alpha = 0.4$ and $\delta = \varepsilon$. We continue the quasi-periodic solutions using the full-discretisation method for the two cases $b = 0$, $\varepsilon \in [0, 2]$ and $b = 1$, $\varepsilon \in [0, 1.2]$. As a start solution for $\varepsilon = 0$ we chose the Fourier series of the function $(x, \dot{x}, y, \dot{y}) = 3(\cos\theta_1, -\sin\theta_1, -\cos\theta_2, \sin\theta_2)$ together with the initial values $\omega_1 = 1$ and $\omega_2 = \sqrt{2}$ for the unknown basic frequencies. This seed solution was used both for $b = 0$ and $b = 1$. As before, we stopped the Newton iteration as soon as the Euclidean norm of the Newton correction falls below 10^{-6}.

Figure 21 shows how the convergence behaviour of our method depends on ε for both cases $b = 0$ and $b = 1$. The top panels show the estimated values of the residual and the bottom panels the rotation numbers $\varrho = \omega_1/\omega_2$. For increasing ε the residual grows rapidly and the algorithm converges slower due to the increasingly complicated geometry of the tori; see Figs. 22 and 23. This worsening of the convergence can also be seen in the contour plots of the norms of the Fourier coefficient vectors in the bottom panels of Figs. 22 and 23. For smaller ε we see an island structure indicating fast convergence. For larger ε, a band of slowly decaying Fourier coefficients close to $3N_1 \approx 2N_2$ for $b = 0$ and $N_1 \approx N_2$ for $b = 1$ emerges. For $b = 1$ we observe a 3:4 and 4:5 sub-harmonic resonance indicated by the formation of a Devil's staircase in the bottom left panel in Fig. 21. Compared with the corresponding graphs in [13, 29], there is a slight difference, because the Devil's staircase structure is not visible for $b = 0$. This may be due to an insufficient accuracy.

Figure 22 shows the approximations of the tori for $b = 0$ and $\varepsilon = 0.65$ or

Figure 22: Approximations of the invariant tori of the system of two coupled Van der Pol oscillators (38)-(39) with $b = 0$ and $\varepsilon = 0.65$ (left panels) or $\varepsilon = 1.65$ (right panels) one the mesh $N_1 \times N_2 = 15 \times 10$. The first oscillator is depicted in the top and the second oscillator in the middle panels. The green curves indicate cross-sections for $\theta_1 = 0$ (top) and $\theta_2 = 0$ (middle). The contour plots in the bottom panels illustrate the decay of the Fourier coefficients and the worsening of the convergence for increasing ε; compare Fig. 23.
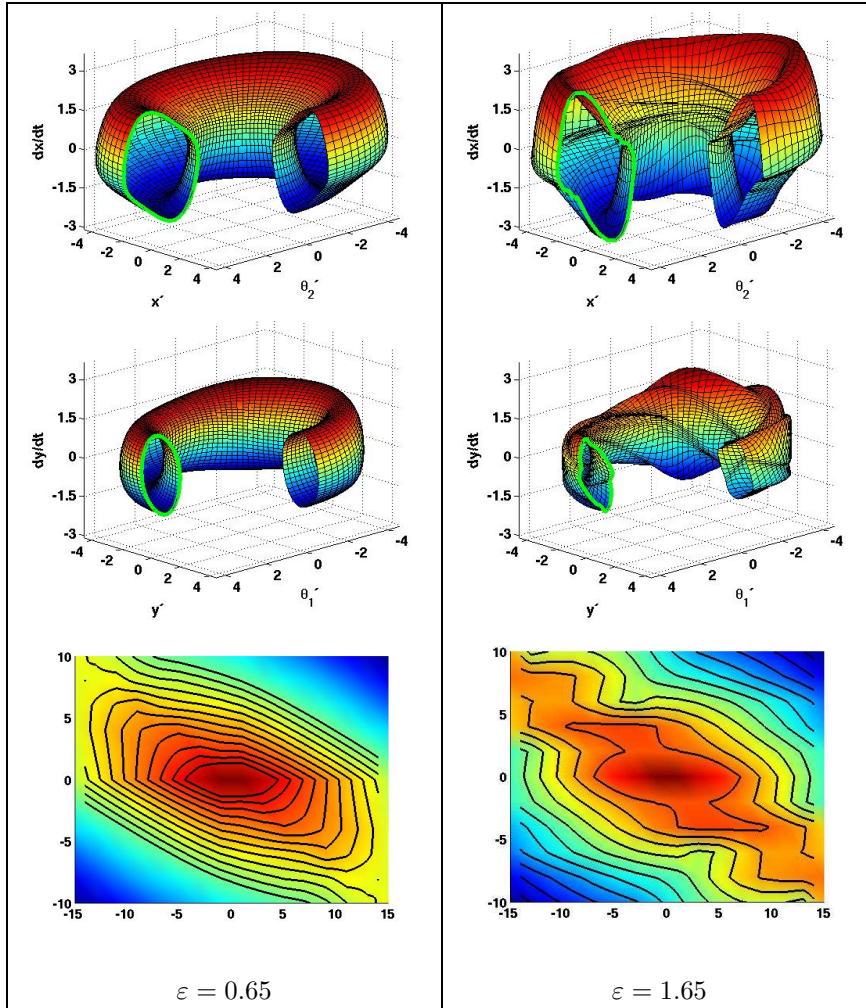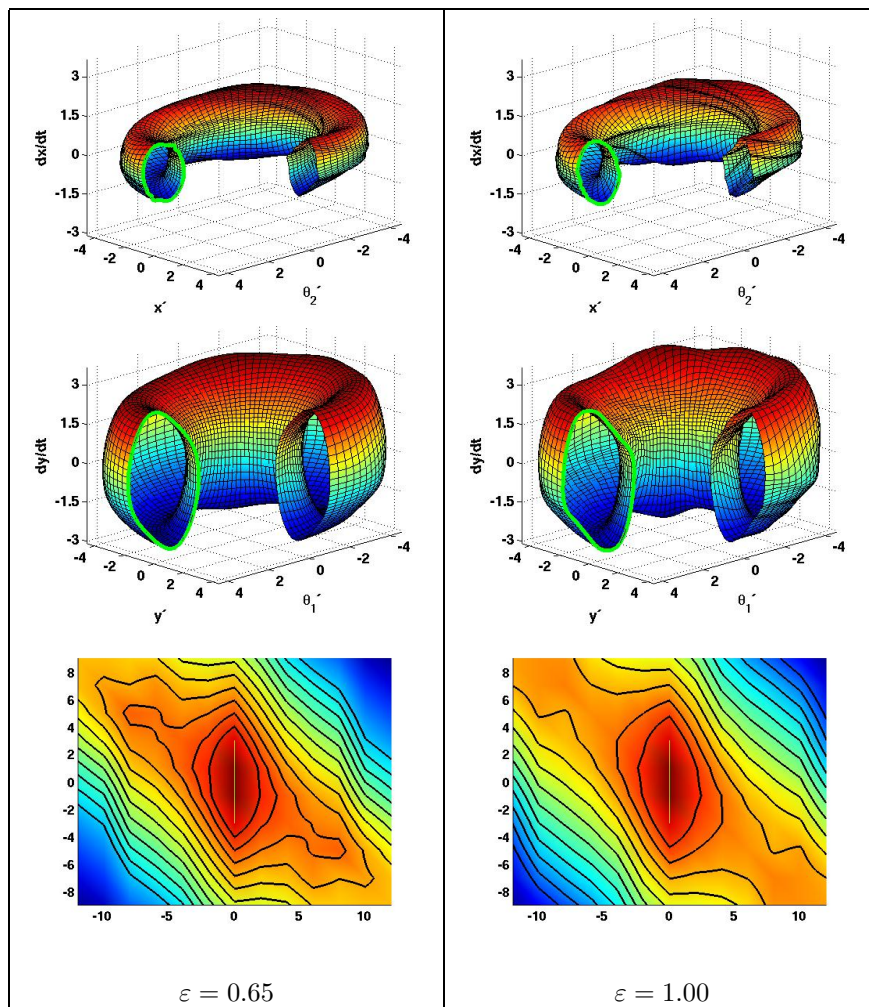
Figure 23: Approximations of the invariant tori of the system of two coupled Van der Pol oscillators (38)-(39) with $b = 1$ and $\varepsilon = 0.65$ (left panels) or $\varepsilon = 1.00$ (right panels) on the mesh $N_1 \times N_2 = 13 \times 9$. The first oscillator is depicted in the top and the second oscillator in the middle panels. The green curves indicate cross-sections for $\theta_1 = 0$ (top) and $\theta_2 = 0$ (middle). The contour plots in the bottom panels illustrate the decay of the Fourier coefficients and the worsening of the convergence for increasing ε; compare Fig. 22.

	$N_1 = 1$		$N_1 = 3$		$N_1 = 5$		$N_1 = 7$		$N_1 = 9$	
	eval.	tot.	eval.	tot.	eval.	tot.	eval.	tot.	eval.	tot.
$N_2 = 3$	0.3	1.2	0.6	0.9	0.8	1.3	1.1	1.7	1.3	2.3
res.	1.55e-01		1.38e-01		1.38e-01		1.38e-01		1.38e-01	
$N_2 = 9$	0.6	1.0	1.3	2.3	2.1	4.3	2.8	7.2	3.5	11.4
res.	1.38e-01		4.92e-02		4.71e-02		4.70e-02		4.70e-02	
$N_2 = 15$	0.9	1.6	2.2	4.5	3.3	11.0	4.5	20.2	5.8	36.2
res.	1.40e-01		2.04e-02		1.06e-02		1.05e-02		1.05e-02	
$N_2 = 21$	1.2	2.1	2.8	7.8	4.6	21.2	6.3	45.1	8.1	85.1
res.	1.40e-01		1.97e-02		5.01e-03		2.16e-03		2.02e-03	
$N_2 = 27$	1.4	3.3	3.5	12.7	5.6	37.1	8.0	85.5	10.1	164.1
res.	1.39e-01		1.97e-02		4.85e-03		1.10e-03		4.16e-04	

Table 4: Computation times for computing the quasi-periodic solutions of the parametrically forced network (15) and associated values of the residual for $\varepsilon = 2.0$ and different orders N_1 and N_2 of the Fourier polynomials.

$\varepsilon = 1.65$. Figure 23 shows the approximations for $b = 1$ and $\varepsilon = 0.65$ or $\varepsilon = 1.0$. In both figures the tori are embedded into $\mathbb{R}^6$ by the change of coordinates

$$\begin{aligned} \theta_2' &= r + x\cos\theta_2, & x' &= r + x\sin\theta_2, & dx/dt &= \dot{x}, \\ \theta_1' &= r + y\cos\theta_1, & y' &= r + y\sin\theta_1, & dy/dt &= \dot{y}, \end{aligned}$$

and projected onto the three-dimensional subspaces $(\theta_2', x', dx/dt)$ in the top panels and $(\theta_1', y', dy/dt)$ in the middle panels. Again r controls the main torus radius and we used $r = 4$ here. Our algorithm produces good approximations of the tori as long as ε remains relatively small. For larger ε the tori develop bulges and it seems that their geometry cannot be fully resolved with the chosen discretisation order. Note that the bulges in the tori in Fig. 22 middle right and Fig. 23 top right seem so large that the tori are no longer parametrisable in polar coordinates. Hence, the self-intersection observed in [13, 29] could be an artifact of the a-priori coordinate transformation and the chosen projection (a normally hyperbolic torus cannot self-intersect [23]). This would also explain some differences in the graphs of the rotation number. However, note that some of these differences may be due to the rather low accuracy of our computations for larger values of ε.

6.4 Performance of the Full-Discretisation Method

Table 4 shows the computation times and values of the residual for the parametrically forced network (15) with $\varepsilon = 2.0$. Table 5 shows the same for the resonant circuit with saturable inductors (19)-(22) with $k_1 = 0.09$. In both tables we varied the order of the Fourier polynomials in the θ_1- as well as the θ_2-direction. The tables show three values in each row and column, indicating the time spent on evaluating the right-hand side of the ODE and its Jacobian (eval.), the total computation time for solving the discretised system (tot.) and the value of the residual (res.). The computation time is approximately proportional to $(nN_1N_2)^3$ and exponential convergence can be observed in the diagonal entries of the residuals. These results were obtained with MATLAB V6.5 R13 on an AMD Duron CPU 900 MHz.

	$N_1 = 1$ eval. tot.	$N_1 = 3$ eval. tot.	$N_1 = 5$ eval. tot.	$N_1 = 7$ eval. tot.	$N_1 = 9$ eval. tot.
$N_2 = 1$	0.1 0.9	0.2 0.5	0.4 0.6	0.5 0.8	0.6 1.0
res.	2.29e-01	1.28e-01	1.28e-01	1.28e-01	1.28e-01
$N_2 = 5$	0.4 0.6	0.9 1.4	1.5 2.3	2.0 3.5	2.6 5.0
res.	1.14e-01	3.61e-03	1.53e-03	1.54e-03	1.55e-03
$N_2 = 9$	0.6 1.0	1.6 2.7	2.5 5.0	3.5 8.9	4.5 14.5
res.	1.14e-01	3.02e-03	6.33e-05	1.67e-05	1.67e-05
$N_2 = 13$	0.9 1.4	2.2 4.2	3.6 9.5	5.0 18.8	6.3 32.5
res.	1.14e-01	3.03e-03	5.68e-05	9.64e-07	1.69e-07

Table 5: Computation times for computing the quasi-periodic solutions of the circuit with saturable inductors (19)-(22) and associated values of the residual for $k_1 = 0.09$ and different orders N_1 and N_2 of the Fourier polynomials.

7   Conclusion

In this paper, we presented two Fourier-Galerkin methods, namely, a semi-discretisation method and a full-discretisation method, for the computation and continuation of quasi-periodic solutions of ODEs. The semi-discretisation method is a two-step method and semi analytical. It uses generalised Fourier polynomials, that is, Fourier polynomials with periodic functions as coefficients for the approximation of a quasi-periodic solution. In a first step, the algorithm sets up a spectral system by deriving a system of ODEs for the coefficient functions. This step is implemented using symbolic algorithms. In a second step the coefficient functions are computed numerically using standard algorithms for periodic solutions of autonomous ODEs. The semi-discretisation method can be regarded as a generalisation of both the method of averaging and the harmonic (spectral) balance method.

The full-discretisation method is a entirely numerical algorithm that computes Fourier polynomial approximations of quasi-periodic invariant tori, the underlying configuration on which quasi-periodic oscillations take place. It is a black-box algorithm that only requires the definition of the right-hand side of the ODE but no further a-priori knowledge. In particular, this method does not depend on the assumption that the quasi-periodic invariant torus can be parametrised in radius-angle coordinates. The full-discretisation method can be regarded as a generalisation of the harmonic (spectral) balance method to the non-response case. Both methods are robust in the sense that they can continue through regions of sub-harmonic resonance (phase-lock) although their derivation was strictly justified for quasi-periodic solutions only, and the computed tori may be inaccurate in these regions.

Furthermore, these methods are independent of the stability type of the quasi-periodic solution or the quasi-periodic invariant torus, respectively. This means that we can follow a branch of tori through a bifurcation where the torus loses its stability. Note that after such a bifurcation the unstable torus can no longer be observed in simulations. Therefore, this method enables a more rapid parametric analysis of existence of invariant tori where previously only ad-hoc simulation or averaging was used.

We extensively investigated quasi-periodic oscillations in various examples

from nonlinear electrical engineering using qualitative (geometric) dynamical systems methods in conjunction with the above algorithms. In particular, we reproduced numerical results that were previously obtained with different methods. The existence of quasi-periodic and sub-harmonic (phase-locked) oscillations was demonstrated and the underlying invariant tori, depending on external parameters, were computed. Here, the quasi-periodic and the sub-harmonic regimes were identified and the co-existence of several solutions illustrated.

8   Acknowledgements

9   Contact

Frank Schilder, Bristol Centre for Applied Nonlinear Mathematics, Department of Engineering Mathematics, University of Bristol, Bristol BS8 1TR, UK (f.schilder@bristol.ac.uk)

Hinke M. Osinga, Bristol Centre for Applied Nonlinear Mathematics, Department of Engineering Mathematics, University of Bristol, Bristol BS8 1TR, UK (h.m.osinga@bristol.ac.uk)

Werner Vogt, Technische Universität Ilmenau, Fakultät für Mathematik und Naturwissenschaften, Postfach 100565, 98684 Ilmenau, Germany (werner.vogt@mathematik.tu-ilmenau.de)

Stephan Schreiber, Technische Universität Ilmenau, Fakultät für Mathematik und Naturwissenschaften, Postfach 100565, 98684 Ilmenau, Germany (stephan.schreiber@stud.tu-ilmenau.de)

References

[1] A. BONDESON, E. OTT AND T. M. ANTONSEN, *Quasiperiodically forced damped pendula and Schrödinger equations with quasiperiodic potentials: Implications of their equivalence*, Phys. Rev. Lett., 55 (1985), pp. 2103–2106.

[2] D.-R. HE, W. J. YEH AND Y. H. KAO, *Transition from quasiperiodicity to chaos in a Josephson junction analog*, Phys. Rev. B, 30 (1984), pp. 172–178.

[3] G. A. HELD AND C. JEFFRIES, *Quasiperiodic transitions to chaos of instabilities in an electron-hole plasma excited by AC perturbations at one and at two frequencies*, Phys. Rev. Lett., 56 (1986), pp. 1183–1186.

[4] D.G. ARONSON, M.A. CHORY, G.R. HALL AND R.P. MCGEHEE, *Bifurcations from an invariant circle for two-parameter families of maps of*

the plane: A computer-assisted study, Commun. Math. Phys., 83 (1982), pp. 303–354.

[5] H.W. Broer, H.M. Osinga and G. Vegter,*Algorithms for computing normally hyperbolic invariant manifolds*, Z. angew. Math. Phys., 48(3) (1997), pp. 480–524.

[6] J.A. Glazier and A. Libchaber, *Quasi-periodicity and dynamical systems*: *An experimentalists view*, IEEE Trans. Circ. Sys., 35(7) (1988), pp. 790–809.

[7] W. de Melo and S. van Strien, *One-Dimensional Dynamics*, Springer Verlag Berlin Heidelberg, 1993.

[8] R. de la Llave, *A tutorial on KAM theory*, in Smooth ergodic theory and its applications (Seattle, WA, 1999), Proc. Sympos. Pure Math., 69, Amer. Math. Soc., Providence, RI, 2001, pp. 175–292.

[9] A.M. Samoilenko, *Elements of the Mathematical Theory of Multi-Frequency Oscillations*, Isdatelstvo Nauka, Moskva 1987; English translation, Kluwer Academic Publishers, Dordrecht et al., 1991.

[10] F. Schilder, H.M. Osinga, W. Vogt, *Continuation of quasi-periodic invariant tori*, to appear in SIAM J. Appl. Dyn. Sys.

[11] A. Dhooge, W. Govaerts and Yu.A. Kuznetsov, *MATCONT: a MATLAB package for numerical bifurcation analysis of ODEs*, ACM Trans. Math. Software, 29(2) (2003), pp. 141–164.

[12] E.J. Doedel, A.R. Champneys, Th.F. Fairgrieve, Y.A. Kuznetsov, B. Sandstede and X. Wang, *AUTO 97*: *Continuation and Bifurcation Software for Ordinary Differential Equations (with HomCont)*, 1997.

[13] Y. Chen, A.Y.T. Leung, *Bifurcation and Chaos in Engineering.* Springer-Verlag London, 1998.

[14] J. Guckenheimer and P. Holmes, *Nonlinear Oscillations, Dynamical Systems and Bifurcation of Vector Fields*, Springer-Verlag Berlin, 1997.

[15] T.S. Parker and L.O. Chua, *Practical Numerical Algorithms for Chaotic Systems*, Springer-Verlag New York, 1989.

[16] J.A. Sanders, F. Verhulst, *Averaging Methods in Nonlinear Dynamical Systems*, Springer Verlag, 1985.

[17] P. Lochak, C. Meunier, *Multiphase averaging for classical systems: with applications to adiabatic theorems*, Springer, 1988.

[18] J.A. Murdock, *Perturbations, Theory and Methods*, John Wiley & Sons, 1991.

[19] F. Schilder, *TorCont: computation and continuation of quasi-periodic invariant tori*, software package, http://www.dynamicalsystems.org/sw/sw/detail?item=44.

[20] E. Philippow and W.G. Büntig, *Analyse nichtlinearer dynamischer Systeme der Elektrotechnik*: *Einführung in die numerische Untersuchung einfacher Systeme*, Carl Hanser Verlag München et al., 1992.

[21] C. Hayashi, *Quasi-periodic oscillations in non-linear control systems*, in Selected Papers on Nonlinear Oscillations, Chihiro Hayashi, Professor Emeritus, Kyoto University; Kyoto University 1975, Printed by Nippon Printing and Publishing Company, Ltd. Yoshino, Fukushima-ku, Osaka, Japan.

[22] D.G. Aronson, M.A. Chory, G.R. Hall and R.P. McGehee, *Resonance phenomena for two-parameter families of maps of the plane: uniqueness and nonuniqueness of rotation numbers*, in Nonlinear dynamics and turbulence pp. 35–47, Interaction Mech. Math. Ser., Pitman, Boston, MA, 1983.

[23] M.W. Hirsch, C.C. Pugh, M. Shub, *Invariant manifolds*, Lecture Notes in Mathematics, Vol. 583. Springer-Verlag Berlin-New York, 1977.

[24] T. Yoshinaga and H. Kawakami, *Bifurcations and chaotic state in forced oscillatory circuits containing saturable inductors*, In: T. Carroll and L. Pecora, Nonlinear Dynamics In Circuits, pp. 89–118, World Scientific Publishing, 1995.

[25] A. Arnéodo, P.H. Coullet and E.A. Spiegel, *Cascade of period doublings of tori*, Phys. Lett. A 94, 1 (1983), pp. 1–6.

[26] J.J. Stagliano, J.-M. Wersinger, E. Slaminka, *Doubling bifurcations of destroyed $\mathbb{T}^2$ tori*, Phys. D 92(3-4) (1996), pp. 164–177.

[27] E. Castellà and À. Jorba, *On the vertical families of two-dimensional tori near the triangular points of the Bicircular problem*, Celestial Mech. 76(1) (2000), pp. 35–54.

[28] À. Jorba, *Numerical computation of the normal behaviour of invariant curves of n-dimensional maps*, Nonlinearity 14(5) (2001), pp. 943–976.

[29] T. Ge and A.Y.T. Leung, *Construction of invariant torus using Toeplitz Jacobian matrices/fast Fourier transform approach*, Nonlinear Dynamics, 15 (1998), pp. 283–305.

[30] H. Mingyou, T. Küpper and N. Masbaum, *Computation of invariant tori by the Fourier methods*, SIAM J. Sci. Comput., 18 (1997), pp. 918–942.